Title

Surface-wave sensitivity to anisotropy in a 3D seismo-geodynamics mantle plume model

-o-

-o-

Authors

Matteo Desiderio (1) | 0000-0003-3060-2961 | ucfbmde@ucl.ac.uk
Ana M. G. Ferreira (1) | a.ferreira@ucl.ac.uk
Stephen P. Hicks (1) | stephen.hicks@ucl.ac.uk
Manuele Faccenda (2, 3) | manuele.faccenda@unipd.it
Francesco Rappisi (4) | francescorappisi@gmail.com
Antonio Manjón-Cabeza Córdoba (1) | a.cordoba@ucl.ac.uk
Maxim D. Ballmer (1) | m.ballmer@ucl.ac.uk

1: Department of Earth Sciences, University College London, London, UK
2: Dipartimento di Geoscienze, Universitá di Padova, Italy
3: Istituto Nazionale di Geofisica e Vulcanologia, Sezione Bologna, Italy
4: European Center for Geodynamics and Seismology, Luxembourg, Luxembourg

submitted to *Geophys. J. Int.*

Surface-wave sensitivity to anisotropy in a 3D seismo-geodynamics mantle plume model

Matteo Desiderio[1], Ana M. G. Ferreira[1], Stephen P. Hicks[1], Manuele Faccenda[2,3], Francesco Rappisi[4], Antonio Manjón-Cabeza Córdoba[1], Maxim D. Ballmer[1]

[1] *Department of Earth Sciences, University College London, London, United Kingdom*

E-mail: matteo.desiderio.20@ucl.ac.uk

[2] *Dipartimento di Geoscienze, Università di Padova, Italy*

[3] *Istituto Nazionale di Geofisica e Vulcanologia, Sezione Bologna, Italy*

[4] *European Center for Geodynamics and Seismology, Luxembourg, Luxembourg*

Received ...; in original form...

SUMMARY

High-resolution anisotropic seismic images of the upper mantle provide fundamental constraints on mantle plume dynamics and mantle deformation. Seismic tomography has come far by using travel-time and waveform (phase) information but has exploited amplitude information only to a limited extent. Here, we calculate adjoint sensitivity kernels to assess the value of incorporating amplitude information and to identify the elastic parameters that most effectively characterise mantle plumes in the uppermost mantle. We first compute strain-induced mineral fabrics and the resulting full elastic tensor in a realistic 3D mantle plume setting. Then, full-waveform computations are carried out within this medium to obtain kernels for fundamental-mode Rayleigh- and Love-wave amplitude (and phase) measurements for all the 21 elastic parameters controlling seismic anisotropy. Finally, we explore the sensitivity of combined observables, such as Rayleigh-wave cross-component phase-delay differences and horizontal/vertical amplitude ratios (i.e., Rayleigh wave ellipticity). Our gallery of phase and amplitude surface-wave adjoint kernels reveals strong and complex sensitivity of these measurements to shear-wave radial anisotropy and to second- and fourth-degree azimuthal anisotropy parameters. We further show that amplitude measurements are highly sensitive to the same elastic tensor components as phase measurements, but with distinct spatial sensitivity patterns that complement phase measurements and strengthen constraints in anisotropic tomography inversions. We find that our combined observables maximize sensitivity beneath and near receivers, highlighting their potential for constraining mantle flow in settings with sparse or logistically challenging instrumentation, such as in oceanic domains.

Key words: Anisotropy – Mantle Plumes – Amplitude kernels – Adjoint method.

1 INTRODUCTION

Earth's upper mantle lies at the critical interface between the deeper convective system and surface tectonic and volcanic processes, ultimately controlling thermal and chemical exchanges that impact Earth's habitability (Foley & Driscoll 2016). Surface-wave seismic tomography is a key tool to constrain the upper mantle's thermochemical structure. Indeed, surface waves, when used either alone or combined with body waves, have been instrumental in mapping the upper mantle (Woodhouse & Dziewonski 1984; Montagner & Tanimoto 1991; Heintz et al. 2005; Sebai et al. 2006; Ritsema et al. 2011; Lekić & Romanowicz 2011; Chang et al. 2015), often illuminating the lithosphere and asthenosphere, as well as mid-ocean ridges, and sub-hotspot mantle plume dynamics (Ye et al. 2022; Debayle & Kennett 2000; Dunn & Forsyth 2003; Mathar et al. 2006; Laske et al. 2011; Gung et al. 2003; Debayle et al. 2016). Surface waves are sensitive to seismic anisotropy in the upper mantle (e.g., Chang et al. 2014), which arises primarily from crystallographic preferred orientations within mineral fabrics (Karato et al. 2008). Because these fabrics can record the direction and geometry of mantle deformation associated with convective flow, surface-wave anisotropic seismic tomography provides a key diagnostic of upper-mantle geodynamics. However, several challenges remain with surface wave imaging.

One challenge is that sub-optimal data-coverage limits the resolution and reliability of tomographic images (e.g., Chang et al. 2014; Fichtner et al. 2024). While complementary multifrequency measurements can be used to mitigate this issue (Ye et al. 2022; Chang et al. 2014), the use of simplified secondary measurements, such as travel times and phase and group velocities, remains widespread (Bozdağ et al. 2011; Chang et al. 2014). While these quantities provide valuable constraints, they distill complex seismic waveforms into a small number of summary parameters, leaving much of the information contained in the full waveforms—including amplitude variations—unexploited (Lekić & Romanowicz 2011; Bozdağ et al. 2011; Fichtner et al. 2008, 2024). Amplitude measurements are a key missing link because they are sensitive to both attenuation and small-scale lateral variations in elastic structure (Romanowicz 1987; Zhou 2009; Dalton & Ekström 2006; Selby & Woodhouse 2000). While the effects of isotropic elastic anomalies on amplitudes is well understood (e.g., Romanowicz 1987; Dalton et al. 2014), the sensitivity of surface wave amplitudes to both radial and azimuthal anisotropy has yet to be systematically studied.

Another challenge is that approximations in the theoretical frameworks that support inversions are still widely used (Chang et al. 2014). In particular, ray theory is commonly used to derive surface-wave sensitivity kernels for computational efficiency, but is not accurate to sub-wavelength structure (Zhou et al. 2005, 2006). More sophisticated approximations can capture diffraction and mode-coupling effects stemming from the finite frequency nature of the wavefield (both in 2D and 3D: see, e.g., Li & Romanowicz 1995; Dahlen et al. 2000; Zhou et al. 2004). However, these approximations become computationally costly when adapted to a three-dimensional reference model (Zhou et al. 2006) and break down in a strongly laterally heterogeneous medium, such as in the crust (Chang et al. 2014; Fichtner et al. 2024; Zhou et al. 2006). More recently, the development of the adjoint method in the context of passive seismology has allowed waveform inversions that honour both small-scale heterogeneities and finite-frequency effects, leading to the first-generation of regional and global adjoint waveform tomographic models (e.g., Thrastarson et al. 2024; Bozdağ et al. 2016; Zhu et al. 2012).

A final issue is that a mitigation to ill-posed inverse problems is often to limit the number and variety of physical parameters considered (e.g., Del Piccolo et al. 2024; Chang et al. 2014; Fichtner et al. 2024), such as for example ignoring the effects of anisotropy. Several approaches have been proposed to discard parameters based on predicted sensitivities, or to design optimal observables that reduce inter-parameter tradeoffs (e.g., Sieminski et al. 2009; Bernauer et al. 2014). However, waveform amplitudes are typically not considered in such analyses.

To progress beyond these challenges and demonstrate the value added by amplitude data, in this study we calculate finite-frequency, surface-wave amplitude kernels using the adjoint method for all the twenty-one coefficients of the elastic tensor, using a 3D, fully anisotropic seismo-geodynamic model of a realistic mantle plume setting. This provides a key physics-driven test to advance future seismic imaging studies of the multi-scale anisotropic structure of mantle upwellings. The aim of this paper is to investigate whether and how surface wave amplitudes are sensitive to variations in anisotropy, and whether they provide complementary or contrasting information to phase information. We also show examples of how to combine observables in order to localize sensitivity in space, thus reducing inter-parameter tradeoffs.

2 THEORETICAL BACKGROUND

2.1 Asymptotic Theory of Anisotropy

To provide a framework for interpreting our results, we first briefly present a ray-theory formulation of seismic anisotropy. According to asymptotic theory, the effect of weak anisotropy can be modelled by adding a small anisotropic perturbation to the elastic tensor of an isotropic, laterally homogeneous Earth model (Smith & Dahlen 1973; Larson et al. 1998). In such a weakly anisotropic, spherical medium, the phase velocity variation $\delta c/c$ (relative to the isotropic case) for surface waves can be expressed as the Fourier series (Larson et al. 1998):

$$\delta c/c = \sum_{n=0,2,4} a_n cos(n\zeta) + b_n sin(n\zeta) \tag{1}$$

where the local azimuth ζ is measured anti-clockwise from the south. The coefficients a_n, b_n are depth-integrals of the surface wave, isotropic radial eigenfunctions, weighted by different asymptotic parameters (depending on whether the surface wave considered is a Love or Rayleigh wave) (Smith & Dahlen 1973; Larson et al. 1998; Chen & Tromp 2007). These asymptotic parameters can be expressed as linear combinations of the components of the elastic tensor C_{ijkl} (see Table A1). For Rayleigh waves, propagation in a weakly anisotropic medium is governed by thirteen

Love Parameters	
A	$V_{Ph}^2\rho$
C	$V_{Pv}^2\rho$
N	$V_{Sh}^2\rho$
L	$V_{Sv}^2\rho$
F	$\eta(V_{Ph}^2 - V_{Sv}^2)\rho$

Table 1. Love parameters describing radial anisotropy expressed in terms of wave speeds and density. The parameter F is often expressed in terms of η, a non-dimensional quantity affecting the propagation of Ph and Sv waves with oblique incidence angles, and controlling the dispersion of Rayleigh waves (Anderson 1965; Dziewonski & Anderson 1981; Song & Kawakatsu 2012).

elastic parameters. Five of these parameters govern radial anisotropy (i.e., for $n = 0$) and correspond to the Love parameters $A,\ C,\ N,\ L$ and F (Smith & Dahlen 1973; Love 1911): for example, A is proportional to the velocity V_{Ph}^2 of a horizontally polarized compressional wave. Similar relations for all five Love parameters are summarised in Table 1. The eight remaining parameters affect Rayleigh wave azimuthal anisotropy in degree $n = 2$ ($B_{c,s},\ H_{c,s},\ G_{c,s}$), and in $n = 4$ ($E_{c,s}$). The subscripts $c,\ s$ are related to even and odd azimuthal dependence: the coefficients a_n and b_n in Equation 1 depend on asymptotic parameters with subscripts c and s, respectively. For Love waves, only six parameters are needed: two for radial anisotropy (N and L) and four for azimuthal anisotropy ($G_{c,s}$ and $E_{c,s}$, for $n = 2$ and $n = 4$, respectively). The azimuthal dependence imparted to phase speeds by these parameters is summarised in Table 2.

For body waves, phase velocity corrections due to weak anisotropic perturbations can be ex-

Degree n	Parameter(s)	Anisotropy	Wave
0	$A,\ C,\ L,\ N,\ F$	Radial	Surface/body
1	$J,\ K,\ M$	Azimuthal	Body
2	$B,\ H,\ G$	Azimuthal	Surface/body
3	D	Azimuthal	Body
4	E	Azimuthal	Surface/body

Table 2. Summary of asymptotic parameters, with their effect on azimuthal dependence ($n = 0$ implies only radial anisotropy). The subscripts c and s (indicating the even/oddness of the azimuthal dependence, respectively) are omitted for conciseness.

pressed as a Fourier series similar to Equation 1, but involving odd-degree terms as well (Chen & Tromp 2007): for $n = 1$ and $n = 3$, azimuthal anisotropy is described using the elastic parameters $J_{c,s},\ K_{c,s},\ M_{c,s}$ and $D_{c,s}$, respectively. For example, for horizontally polarized P waves (Chen & Tromp 2007):

$$\delta c/c = \frac{1}{2c^2}(A + B_c cos2\zeta - B_s sin2\zeta + E_c cos4\zeta - E_s sin4\zeta)\rho^{-1} \tag{2}$$

We note that, in general, anisotropic effects for body waves also depend on ray incidence angles.

In this study, kernels are computed with respect to variations in C_{ijkl} components. These kernels are re-combined, so that sensitivities can be more readily understood with respect to the anisotropy parameters introduced above using the linear combinations of Table A1.

2.2 Adjoint Kernels

We compute the sensitivity of seismic observables to variations in the elastic tensor using the adjoint method. The method relies on the simultaneous propagation of the forward and adjoint wavefields to evaluate the Fréchet derivatives with respect to perturbations in the background model. These derivatives, or sensitivity kernels, quantify the response of a given measurement to perturbations in density ρ and in the elastic tensor C_{ijkl} (e.g., Tromp et al. 2005).

Upon imposing such a perturbation, a generic measurement (or observable) d changes, to the first order, by the quantity (Sieminski et al. 2007):

$$\delta d = \int_0^T \delta s_i(\mathbf{x}_r, t) g_i(\mathbf{x}_r, t) dt \tag{3}$$

where t is the time from 0 to T, δs_i is the perturbation on the $i-$th component of the displacement field recorded at the receiver location $\mathbf{x} = \mathbf{x}_r$ (no summation over i is implied in the above). The adjoint source time function g_i takes a different form depending on the specific observable considered (Dahlen & Baig 2002; Tromp et al. 2005):

$$g_i(\mathbf{x}_r, t) = w(t)\frac{1}{N_a} s_i(\mathbf{x}_r, t) \qquad \text{for relative amplitude variations and} \tag{4}$$

$$g_i(\mathbf{x}_r, t) = w(t)\frac{1}{N_\phi} \partial_t s_i(\mathbf{x}_r, t) \qquad \text{for phase delays,} \tag{5}$$

where $w(t)$ is a time-domain window and

$$N_a = \int_0^T w(t) s_i^2(\mathbf{x}_r, t) dt \tag{6}$$

$$N_\phi = \int_0^T w(t) s_i(\mathbf{x}_r, t) \partial_t^2 s_i(\mathbf{x}_r, t) dt \tag{7}$$

are normalization constants. The adjoint source time-functions above imply that phase delays and relative amplitude variations are measured via cross-correlation and ratios between root mean squares, respectively (Dahlen et al. 2000). The wavefield perturbation can be obtained using the Born approximation (e.g., Dahlen et al. 2000; Hung et al. 2000; Tromp et al. 2005):

$$\delta s_i(\mathbf{x}, t) = -\int_0^t \int_\Omega \Big[G_{ij}(\mathbf{x}, \mathbf{x}'; t-t') \delta\rho(\mathbf{x}') \partial_{t'}^2 s_j(\mathbf{x}', t') + \\ + \partial_{x'_k} G_{ij}(\mathbf{x}, \mathbf{x}'; t-t') \delta C_{jklm}(\mathbf{x}') \partial_{x'_l} s_m(\mathbf{x}', t') \Big] d^3\mathbf{x}' dt' \tag{8}$$

where Ω is the total volume of the medium and G is the Green's tensor between the two pairs of points in space $\mathbf{x}$ and $\mathbf{x}'$, and time t and t' (Einstein's convention for repeating indices is used). Because of the Green's tensor reciprocity, $G_{ij}(\mathbf{x}, \mathbf{x}'; t-t') = G_{ji}(\mathbf{x}', \mathbf{x}; t-t')$ and $\partial_{x'_k} G_{ij}(\mathbf{x}, \mathbf{x}'; t-t') = \partial_{x_j} G_{ki}(\mathbf{x}', \mathbf{x}; t-t')$ (Sieminski et al. 2007). Further, by applying the time-reversal $t \to T-t$ and substituting δs_i in Equation 3, δd becomes:

$$\delta d = -\int_0^T \int_\Omega \Big[\delta\rho(\mathbf{x}') \int_0^{T-t} \partial_{t'}^2 s_j(\mathbf{x}', t') G_{ji}(\mathbf{x}', \mathbf{x}_r, T-t-t') g_i(\mathbf{x}_r, T-t) dt' + \\ \delta C_{jklm}(\mathbf{x}') \int_0^{T-t} \partial_{x'_l} s_m(\mathbf{x}', t') \partial_{x_j} G_{ki}(\mathbf{x}', \mathbf{x}_r, T-t-t') g_i(\mathbf{x}_r, T-t) dt' \Big] dt d^3\mathbf{x}' \tag{9}$$

Here, the time-reversed adjoint wavefield can be recognized:

$$s_k^\dagger(\mathbf{x}', T-t') = \int_0^{T-t'} \int_\Omega G_{ki}(\mathbf{x}', \mathbf{x}; T-t'-t) f_i^\dagger(\mathbf{x}, t) dt d^3\mathbf{x} \tag{10}$$

where the wavefield $s_k^\dagger$ is excited by the adjoint source (Tromp et al. 2005; Liu & Tromp 2008):

$$f_i^\dagger(\mathbf{x}, t) = g_i(\mathbf{x}_r, T-t) \delta(\mathbf{x} - \mathbf{x}_r)\,, \tag{11}$$

and δ is the Dirac's distribution. Using the adjoint wavefield in Equation 10, Equation 9 can be rewritten as:

$$\delta d = \int_\Omega \Big[K_\rho(\mathbf{x}) \delta\rho + K_{C_{ijkl}}(\mathbf{x}) \delta C_{ijkl} \Big] d^3\mathbf{x} \;\;, \tag{12}$$

where, after introducing the regular and adjoint strain tensors ϵ and $\epsilon^\dagger$ (Tromp et al. 2005):

$$K_\rho(\mathbf{x}) = -\int_0^T s_i^\dagger(\mathbf{x}, T-t) \partial_t^2 s_i(\mathbf{x}, t) dt \tag{13}$$

and

$$K_{C_{ijkl}} = -\int_0^T \epsilon^{\dagger}_{ij}(\mathbf{x}, T-t)\epsilon_{kl}(\mathbf{x}, t)dt \tag{14}$$

are the sensitivity kernels with respect to absolute (or linear) variations in ρ and C_{ijkl} (kernels with respect to relative variations are not well defined, see Sieminski et al. 2007).

In this study, these kernels are computed by solving numerically for **s** and **s**† using the spectral element code SPECFEM3D_GLOBE (Komatitsch 2010; Tromp et al. 2008). To avoid prohibitive data storage requirements (encountered if both $\mathbf{s}(\mathbf{x}, t)$ and $\mathbf{s}^\dagger(\mathbf{x}, t)$ are saved on disk), the computation is divided into two steps (e.g., Liu & Tromp 2008):

(i) solve for **s** and store $\mathbf{s}(t = T),\ \partial_t\mathbf{s}(t = T)$

(ii) propagate $\mathbf{s}(T-t)$, with the 'initial' conditions saved above, jointly with **s**† forward in time.

For regional simulations with absorbing boundary conditions, step (i) also requires saving the wavefield absorbed at the boundaries at $t = T$ (Liu & Tromp 2008). If anelasticity is taken into account, solving for **s** backward in time also requires to amplify the wavefield in order to reverse attenuation, leading to numerical instability: to overcome this, intermediate wavefield snapshots are stored during step (i), at regular intervals. The checkpoints thus saved are used for the amplitude correction during the back-propagation of **s** in step (ii) (Komatitsch et al. 2016).

2.3 Background Earth Model

The adjoint method is well-suited for computing sensitivities in a 3D background model (e.g., Liu & Tromp 2008). In this study, we adopt synthetic $\{\rho, C_{ijkl}\}$ fields derived from a geodynamic model of a realistic mantle plume setting in the upper-mantle using calculations of strain-induced development of mineral fabrics (Manjón-Cabeza Córdoba & Ballmer 2022; Kaminski et al. 2004; Faccenda et al. 2024). For more details beyond those presented in this section, see Appendix A and Manjón-Cabeza Córdoba & Ballmer (2022).

Conservation of mass, momentum and energy equations are solved with the finite-element code CitcomCU (Moresi & Solomatov 1995). The equations are solved in the extended Boussinesq approximation (Christensen & Yuen 1985), although an adiabatic temperature gradient is imposed

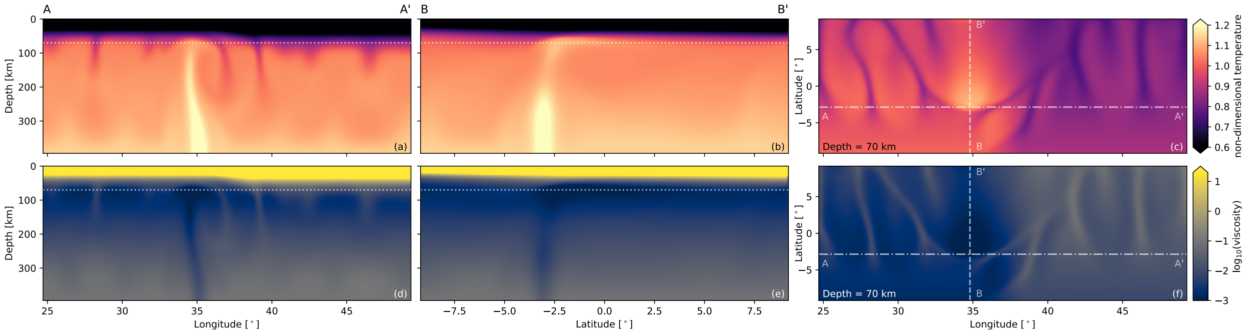

Figure 1. Non-dimensional temperature (top row) and viscosity fields (bottom row) of the input geodynamic plume model, at steady-state, shown along different cross sections. The dotted lines in panels a-b, d-e indicate the depth at which the constant-depth slice of panels c, f is taken ($z = 100$ km). The dot-dashed, and dashed lines in panels c, f indicate the latitude and longitude at which the slices of panel pairs a-b and d-e are taken, respectively.

(Manjón-Cabeza Córdoba & Ballmer 2022). The computational domain spans $2640 \times 1980 \times 660$ km, along the Cartesian axes $\{x, y, z\}$ corresponding to longitude, latitude and depth, respectively, and the reference viscosity is 8.29×10^{18} Pa s. As a boundary condition, a constant velocity $v_{plate} = 2$ cm yr^{-1} towards positive y is imposed at the upper boundary, to model plate motion. Initial conditions include a relatively sharp transition between oceanic and continental litosphere (at $x = 1320$ km). This is modelled via a linear temperature gradient over 264 km (in the x direction) between initial thermal ages of 40 and 100 Ma, respectively (see Fig. 1a, d). The plume is obtained by imposing an initial smooth thermal anomaly of $200°$C at the lower boundary, at a horizontal distance of 200 km from the continental edge (the buoyancy flux is kept constant at 200 kg s^{-1}). At model onset, edge-driven convection (EDC) develops almost immediately, due to the presence of the continental edge. A plume develops from the bottom thermal anomaly, and is deflected ocean-ward by interaction with EDC. When it reaches the base of the lithosphere, it flattens into a pancake (see Fig. 1a), which is then dragged towards positive y by imposed plate motion (see Fig. 1b, c). Stable small-scale convection also develops in time, with Richter rolls alignment parallel to v_{plate} (see Fig. 1c). The model is run until statistical steady-state is achieved.

Development of mineral fabric from strain-induced Crystallographic Preferred Orientation (CPO) is computed using the D-REX_M version of the ECOMAN suite (Kaminski et al. 2004; Faccenda et al. 2024). Upper mantle and mantle transition zone crystal aggregates are regularly

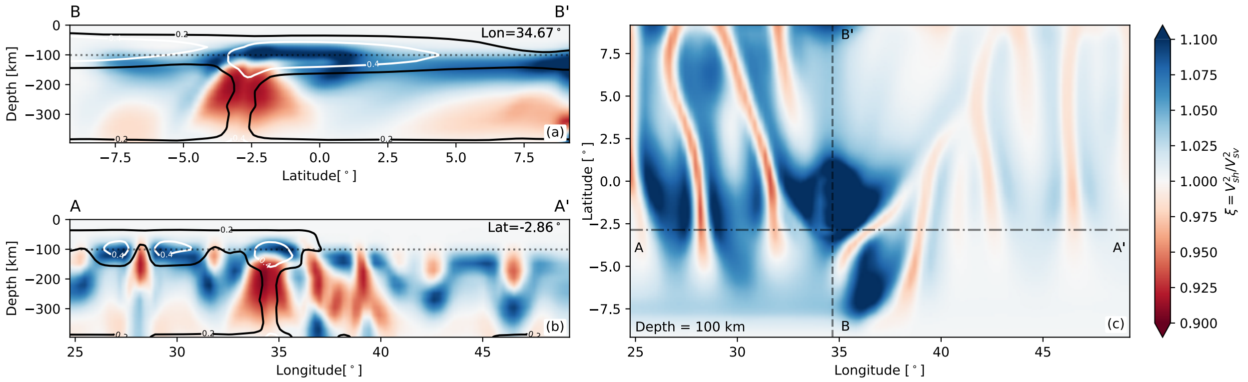

Figure 2. Radial anisotropy in the input model represented by the ξ parameter. To clarify the plume geometry, black and white contour lines indicate the 0.2% and 0.4% negative density anomaly, respectively. The dotted line in panels a, b marks the depth at which the slice of panel c is taken. The dashed and dot-dashed lines in panel c indicate the longitude and latitude at which the slices of panels a and b are taken, respectively.

distributed throughout the computational domain, but fabric evolution is computed only for upper mantle aggregates present to a maximum depth $z = 400$ km. Each Lagrangian tracer– representing multi-crystal, olivine-enstatite mineral aggregates (in 70:30 $\%vol$ proportions) with random starting orientation– tracks upper mantle fabric development in response to the geodynamic model's time-dependent strain field, and assuming dislocation creep entirely accommodates upper mantle deformation. Fabrics are randomised across the olivine-spinel phase transition. D-REX was run using standard model parameters (Boneh et al. 2015), yielding Type-A olivine fabrics with medium strength. The final snapshot of the elastic tensor $C_{ijkl}(\mathbf{x})$ is computed based on a Voigt-Reuss-Hill mean among the crystals, with additional corrections for local pressure/temperature conditions, using thermodynamic look-up tables for a pyrolitic mantle composition (Chust et al. 2017).

Fig. 2 shows radial anisotropy in terms of the ratio $\xi = (V_{Sh}/V_{Sv})^2 = N/L$, where N, L are computed using the $C_{ijkl}(\mathbf{x})$ components obtained from the calculations described above. We observe that $\xi < 1$ corresponds to vertical flow (see, e.g., the plume stem and the Richter rolls), while $\xi > 1$ is associated with horizontal flow (see, e.g., plume pancake), consistent with the assumption of an A-type mineral fabric for the aggregate (Karato et al. 2008; Chang et al. 2014).

Similarly, Fig. 3 shows the azimuthal anisotropy computed from the $C_{ijkl}(\mathbf{x})$ using asymptotic theory. As expected, degree-4 perturbations to Rayleigh-wave phase-velocity are negligible com-

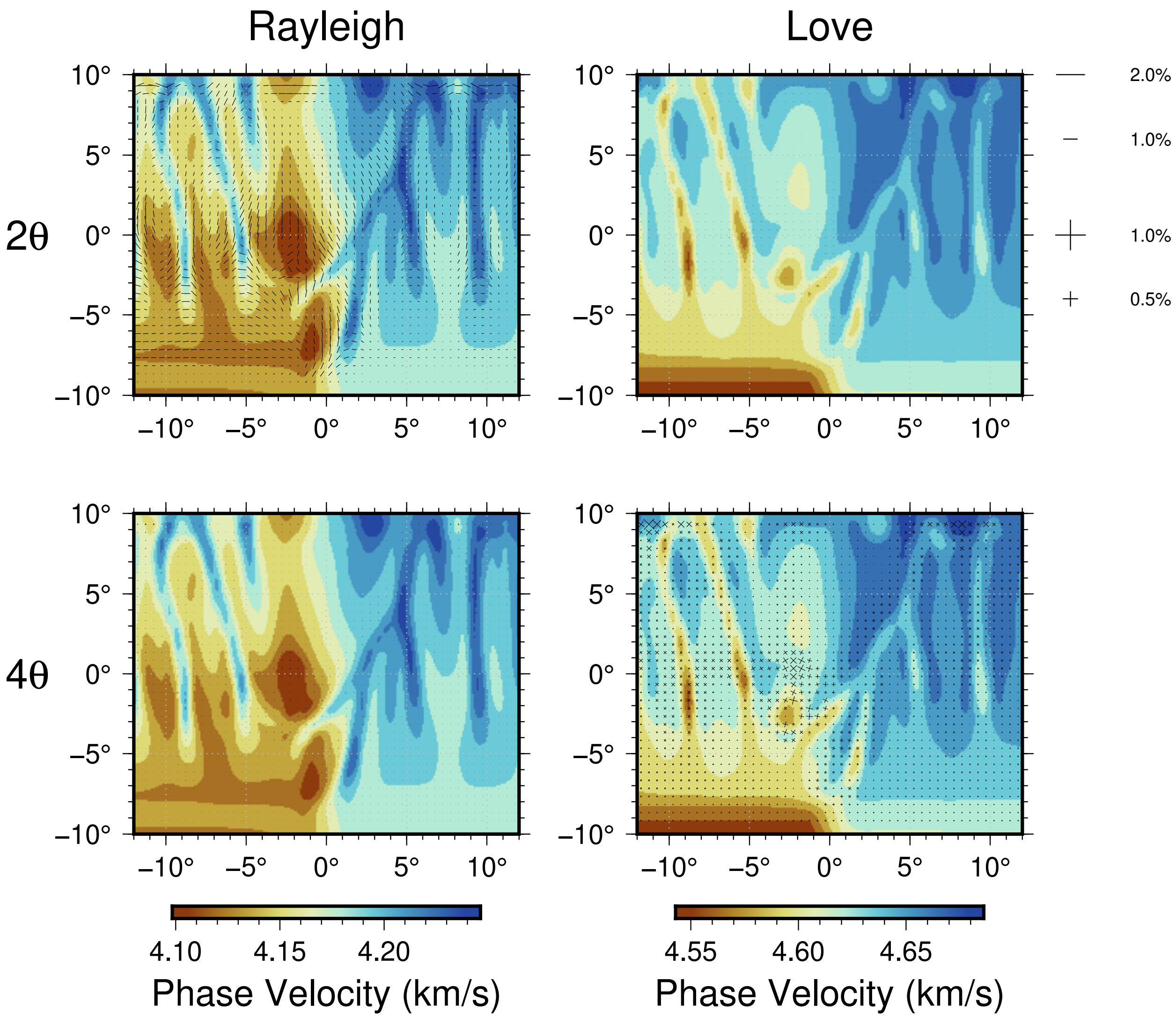

Figure 3. Azimuthal anisotropy for fundamental-mode Rayleigh and Love waves for period $T = 50$ s. Colors indicate phase velocity, while markers represent directions and strength of phase-velocity perturbations due to degree 2 and 4 azimuthal anisotropy, as labelled on the plot and legend.

pared to degree-2 variations, and vice-versa for Love waves (Smith & Dahlen 1973; Montagner & Nataf 1986; Chen & Tromp 2007).

2.4 Model Setup

The $C_{ijkl}(\mathbf{x})$ obtained above is converted from a formulation in Cartesian coordinates to one appropriate for a geographical reference frame. The model is placed within the finite-element mesh between $25°\mathrm{E}{-}49°\mathrm{E}$, $15°\mathrm{S}{-}3°\mathrm{N}$, with the plume pancake oriented towards the South (see Fig. 4), via linear interpolation (a modified version of the SPECFEM3D_GLOBE internal mesher is used,

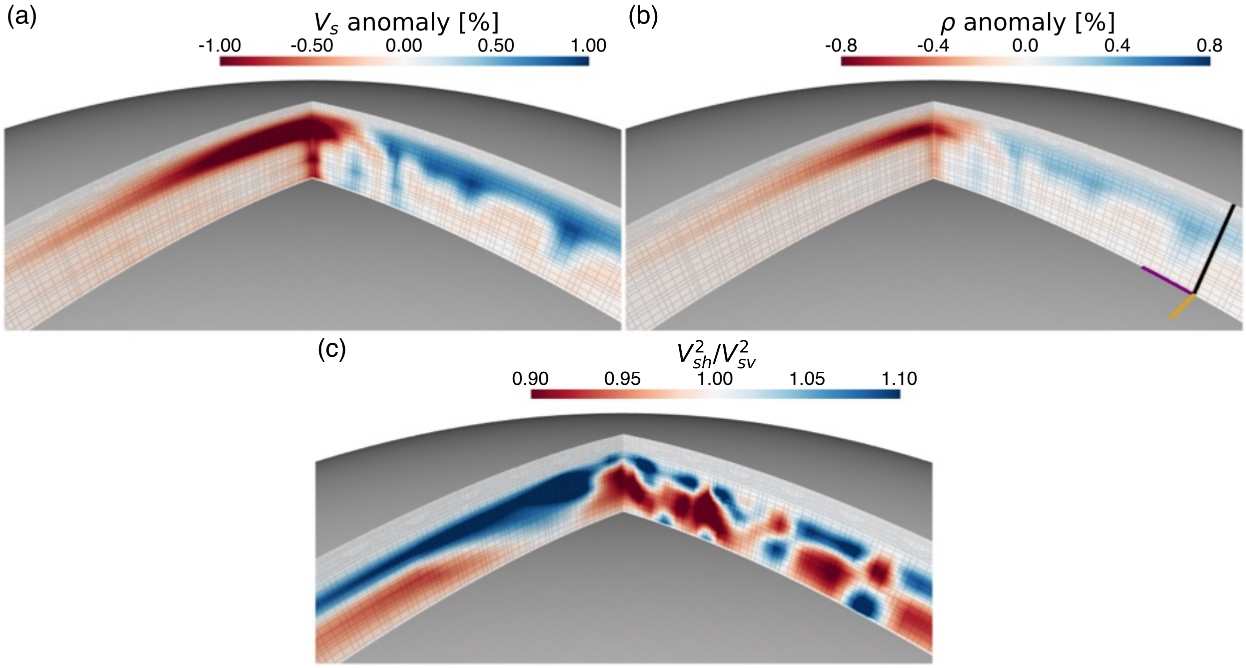

Figure 4. Examples of input model properties (V_s, ρ anomaly and radial anisotropy) within the SPECFEM3D_GLOBE mesh. The density anomaly is calculated with respect to the horizontal average at each depth. The two perpendicular cross-sections shown are aligned to the S-N and E-W directions, and intersect at the plume position (approximately 3°S, 35°E). The vertical black bar length is 400 km. The purple and orange bars point towards west and south, respectively, and are both 2 degrees long.

see Rappisi et al. 2026). Outside of the geodynamic model boundaries, the 3D structure is replaced by a 1D profile corresponding to the horizontal average of the model itself, with a smooth transition between the two. Below 400 km, the isotropic PREM model is used (Dziewonski & Anderson 1981).

The computational domain has a total size of $90°$ and $80°$ along longitude and latitude, respectively. Absorbing boundaries are used. Wavefield calculations are accurate down to a minimum period $T = 30$ s (see Sect. B). Gravity, rotation, ellipticity (as well as oceans and topography) are neglected in our simulations, whereas attenuation is incorporated using three standard linear solids (Komatitsch et al. 2016). The receiver is located west of the plume stem, at coordinates $2.86°$S, $30°$E, to mirror a reasonable scenario in which the location of the plume is only approximately known (and, thus, the receiver is not directly placed above the plume). For Rayleigh and Love wave calculations, we use epicentral distances $35°$ and $50°$, respectively, in order to avoid contamination from other phases in the surface-wave time-window considered. Source mechanisms are pure strike-slip, with the strike oriented such that maximum energy radiates towards the receiver. A schematic view of the computational setup is reproduced in Fig. A2.

Adjoint source time functions obtained using Equations 4, 5 are shown in Fig. A1, along with the displacement in different period bands. The source time functions are calculated and windowed after the original seismograms are band-pass filtered (which also eliminates numerical noise, Komatitsch & Tromp 2002). The period band used in the following is [40, 60] s, and additional computations in the bands [60, 80] s, [80, 120] s are shown in the supplementary materials. For any single component selected for the computation, the other two remaining components of $\mathbf{f}^\dagger$ (Eq. 11) are set to zero. After the kernels are calculated for each elastic constant, they are recombined and presented in terms of asymptotic parameters based on the definitions in Table A1.

3 RESULTS

Here, we present the results of our finite-frequency, adjoint amplitude kernels for the 21 elastic constants, and computed using the 3-D fully anisotropic seismo-geodynamic model presented in Section 2.3. In addition to single model parameter kernels, we also present examples of combined kernels depicting enhanced sensitivity near the receiver. Surface wave phase kernels are collected in the supplementary material (Figs. S7–S15). All kernels are with respect to absolute (or linear) variations in the elastic constants.

3.1 Kernels for Rayleigh wave amplitude measurements

3.1.1 Radial anisotropy parameters

Figs. 5 and S1 show sensitivities of Rayleigh wave fundamental-mode amplitude (measured on the vertical and radial components, respectively) to variations in the radial anisotropy parameters (Love 1911). Panels a-e, show non-zero sensitivity for all Love parameters and strong sensitivity to $A \propto V_{Ph}^2$, particularly in the crust (i.e., for $z \leq 25$ km) and to $L \propto V_{Sv}^2$ at greater depths in the upper mantle (for $z \sim 80$ km). Non-negligible sensitivity is obtained for F as well, at $z \sim 80$ km. Due to the effect of geometrical spreading, the strongest sensitivity is obtained close to the source and the receiver (Zhou et al. 2004). For L and F, a region of high sensitivity extends as deep as the

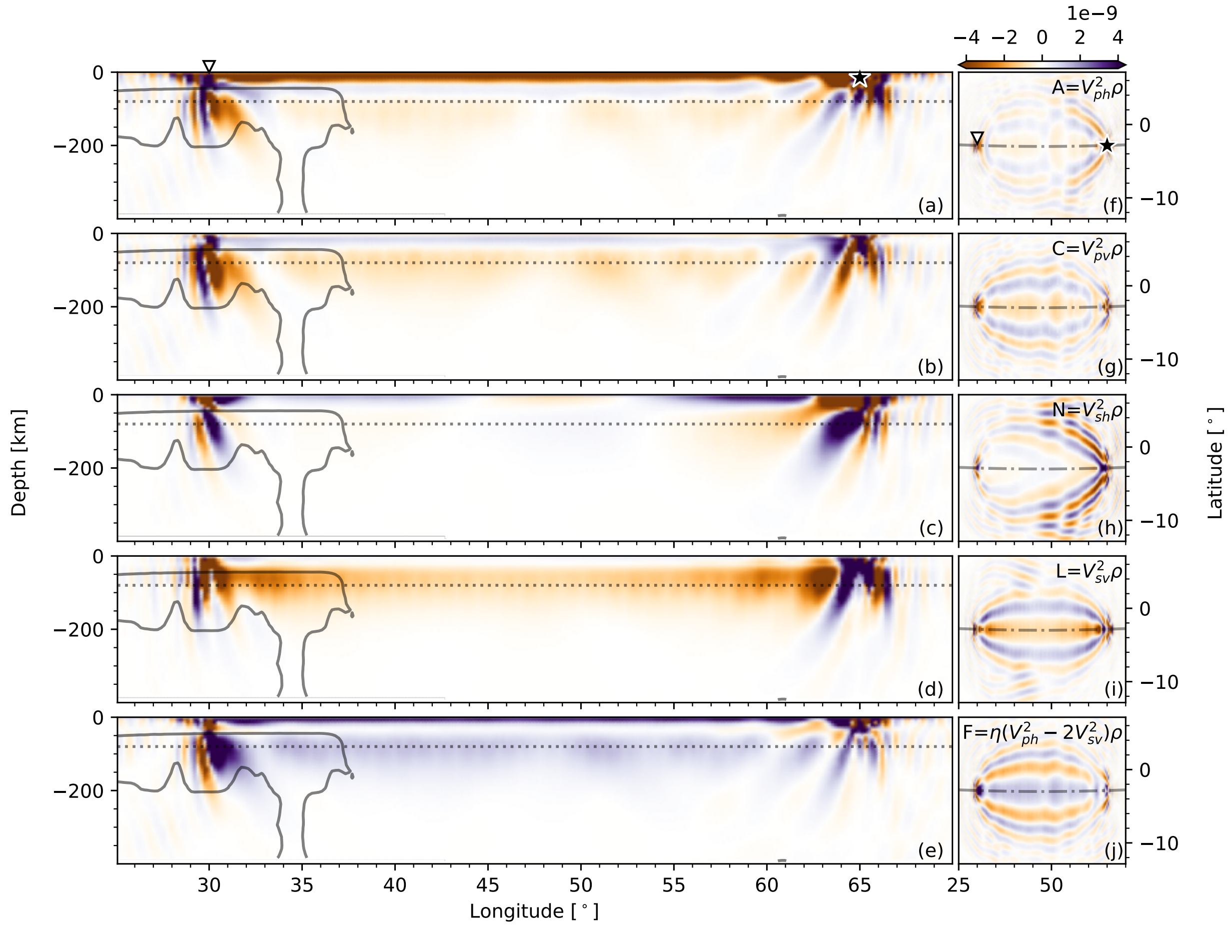

Figure 5. Amplitude kernels of radial anisotropy parameters for fundamental-mode Rayleigh wave measurements made on the vertical component Z, in units GPa^{-1}m^{-3}. The period band for this computation is [40, 60] s. The dotted lines in panels a-e indicate the depth ($\sim$ 80 km) at which the slices in panels f-j are taken. The dot-dashed lines in the f-j panels indicate the latitude at which the sections in panels a-e are shown, corresponding to the source-receiver plane. The source and receiver are marked with a star and a triangle, respectively. The maximum depth shown in the sections is 400 km, and the plume is outlined by contouring the density anomaly at -0.1%.

plume head, but, as depth increases from 80 to 200 km, kernels decay by $\sim$ 2 orders of magnitude. For all other parameters, sensitivity is even more closely focused near the receiver. In all cases, kernel magnitude decreases with depth such that sensitivity to the plume stem is low.

All the kernels (except for N) are characterized by an elliptical shape along the great circle path, with a pattern of successive Fresnel zones alternating constructive-destructive interference from the centre (see the depth slices of Figs. 5, S1f-j). These kernels are also characterised by lateral oscillatory fringes further away from the great circle path (i.e., at distances greater than ~ 5

degrees). Lateral fringes are particularly strong in the N kernel, while no internal ellipse is present (see Fig. 5i). For measurements in the Z component, these fringes appear close to the source. Conversely, in the radial component E, they appear close to both the source and receiver (see, e.g, Fig. S1i). Overall, at the chosen depth $z = 80$ km, amplitude measurements for fundamental mode Rayleigh waves are mostly sensitive to L, F and, more weakly, to C, with higher values concentrated within the first Fresnel zone. High values are obtained for N as well, but only within the lateral fringes far off the great circle path.

3.1.2 Azimuthal anisotropy parameters

Figs. 6 and S2 show the sensitivity of Rayleigh-wave amplitude (vertical and radial component, respectively) to the parameters $B_{c,s},\ H_{c,s},\ G_{c,s}$ (linked to degree 2 variations of ray azimuth ζ) and $E_{c,s}$ (degree 4). In the source-receiver plane, strong kernels are obtained for $B_c,\ H_c,\ G_c$ and E_c, but not for $B_s,\ H_s,\ G_s$ and E_s (see Fig. 6a-d and e-h, respectively). In particular, $B_c,\ H_c,\ E_c$ kernels are especially strong in the crust. For G_c, instead, no sensitivity is obtained in the crust. Further, H_c and G_c exhibit a significant sensitivity peak at $z = 80$ km. Accordingly, only for these two parameters, somewhat high sensitivity is obtained close to the plume head (this depth-dependence is consistent with Sieminski et al. 2007). Moreover, at $z = 80$ km, the patterns of B_c, E_c and H_s, E_s kernels are dominated by lateral fringes near the source, on the vertical component (see Fig. 6i-l). For radial component measurements, kernels exhibit additional fringes close to the receiver (Fig. S2i-l). Instead, only H_c and G_c exhibit a full ellipse extending along the great circle path. In particular, H_c presents both a main ellipse and lateral fringes (Fig. 6i-l). Finally, we note that $B_s,\ H_s,\ G_s$ and E_s kernels are asymmetric with respect to the source-receiver plane (see Figs. 6m-p and S2m-p).

Figs. 7, S3 show sensitivities for the odd-degree azimuthal anisotropy parameters $J_{c,s},\ K_{c,s},\ M_{c,s}$ ($\sim \zeta$) and $D_{c,s}$ ($\sim 3\zeta$). For $J_c,\ K_c,\ M_c$ and D_c, null sensitivity is obtained in the source-receiver plane (Figs. 7a-h, S3a-h. For the other parameters, sensitivities are weak, with some exceptions. For example, relatively strong sensitivities are obtained for J_s, but are confined in the crust. For M_s and D_s, Rayleigh-wave amplitude measurements are mostly sensitive to areas within a ~ 300

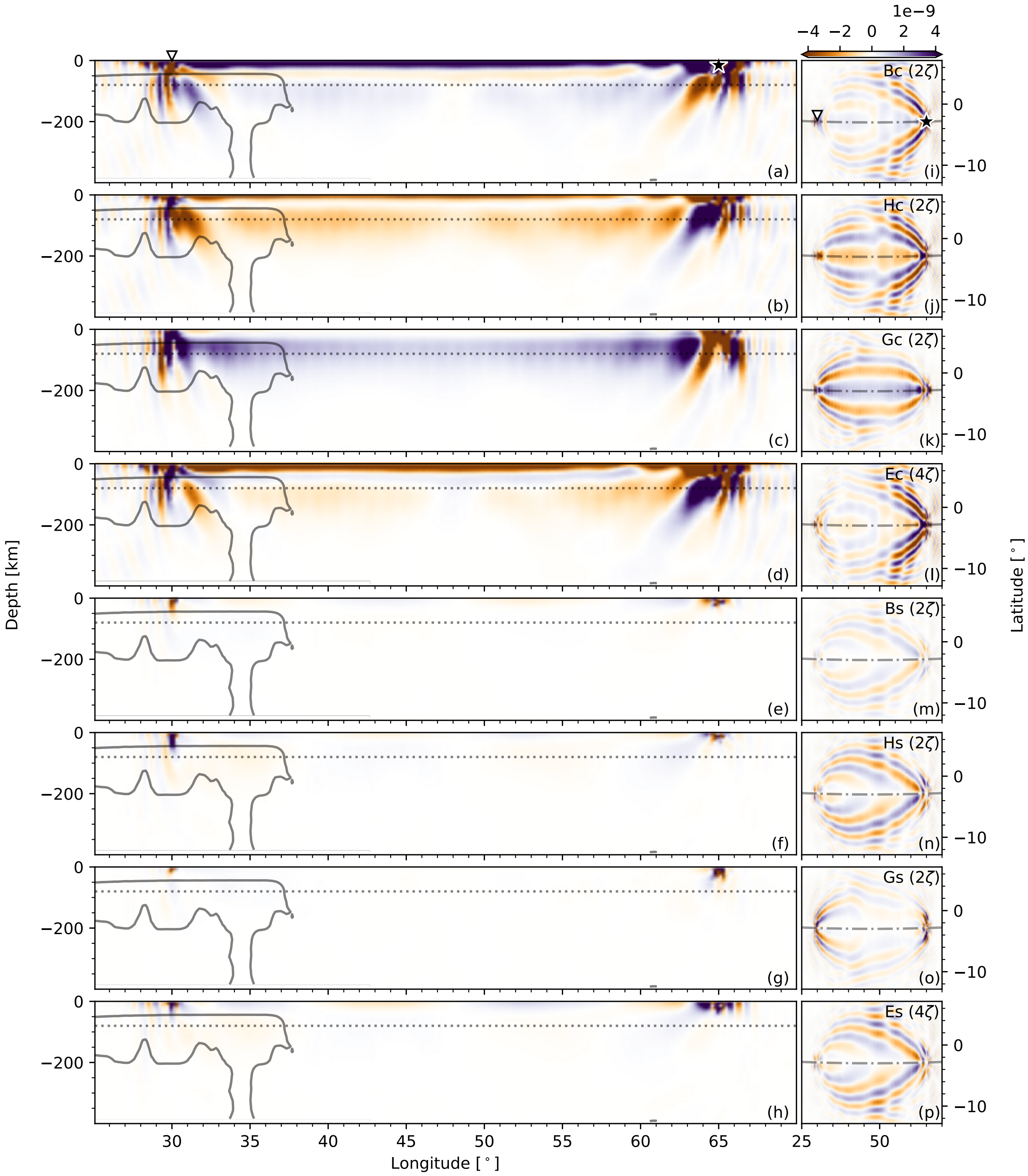

Figure 6. Amplitude kernels of even-degree azimuthal anisotropy parameters for fundamental-mode Rayleigh wave measurements made on the vertical component Z. All other details as in Fig. 5.

km radius around the source and/or receiver. For K_s, sensitivity extends up to $10°$ away from the source and receiver, and up to $z = 150$ km. Thus only for K_s high sensitivity is obtained within the plume head. At $z = 80$ km, none of these parameters exhibits a full ellipse along the great circle path, and most instead present strong oscillatory fringes (see Figs. 7i-p, S3i-p). Conversely,

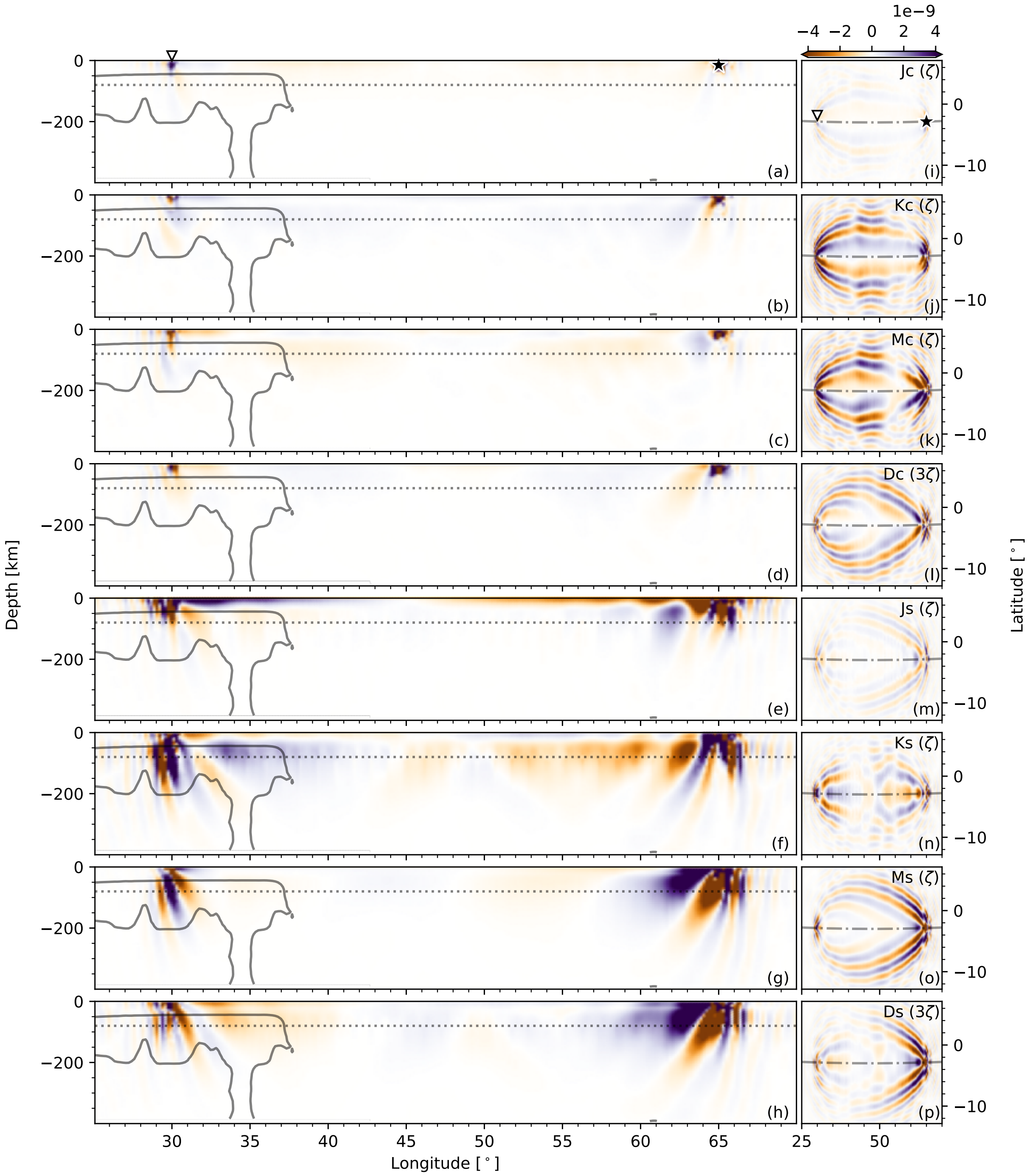

Figure 7. Amplitude kernels of odd-degree azimuthal anisotropy parameters for fundamental-mode Rayleigh wave measurements made on the vertical component Z. All other details as in Fig. 5.

$J_{c,s}$ kernels are characterized by weak fringes. Finally, we once again note that kernel patterns are asymmetrical for the parameters with subscript c (e.g., Fig. 7i-l).

3.2 Kernels for Love wave amplitude measurements

As shown in Fig. 8, fundamental mode, Love-wave amplitude measurements are especially sensitive to N, both in the source-receiver plane and far away from the direct ray path. At $z = 80$ km, for example, sensitivity is concentrated within the first and second Fresnel zones (i.e., between $\pm 5°$N of the source-receiver mid-point). Conversely, sensitivity to variations in L is low and confined within a $\sim$ 200 km radius from the receiver. Among even-degree azimuthal anisotropy parameters, strong and weak sensitivities are obtained for E_c and G_c, respectively (for $z < 80$ km). As for odd-degree parameters, Love-wave measurements have a low sensitivity to $M_{c,s}$ and $D_{c,s}$, for $z < 80$ km. Overall, near the plume head, Love-wave amplitude measurements are thus only sensitive to variations in N and E_c structure. For all the remaining radial and azimuthal anisotropy parameters, sensitivity is virtually null (see Figs. S4 - S6).

4 DISCUSSION

In this study, we presented—for the first time, to our knowledge—adjoint finite-frequency sensitivity kernels of fundamental-mode surface-wave amplitudes with respect to all 21 independent elastic constants, which control radial and azimuthal seismic anisotropy. Therefore, to validate our calculations, we compare our kernels to known results from ray and finite-frequency theory.

4.1 Comparison with asymptotic theory

Asymptotic theory describes surface wave sensitivites within the source-receiver plane (i.e., near the direct ray path, see, e.g., Sieminski et al. 2007). Fundamental-mode Rayleigh waves can be represented as a superposition of P and Sv evanescent waves. Consequently, their sensitivity is particularly strong to the elastic parameters $A \propto V_{Ph}^2$, $L \propto V_{Sv}^2$ and F (Fig. 5a-e), which governs the propagation of P and Sv waves with non-zero incidence angle (e.g., Sieminski et al. 2007; Song & Kawakatsu 2012; Dziewonski & Anderson 1981). Love waves are instead sensitive to $N \propto V_{Sh}^2$ (Fig. 8a).

For Rayleigh waves (Fig. 6), strong kernels are also obtained for B_c, H_c and G_c, as their propagation is controlled by degree-two parameters (Montagner & Nataf 1986; Chen & Tromp

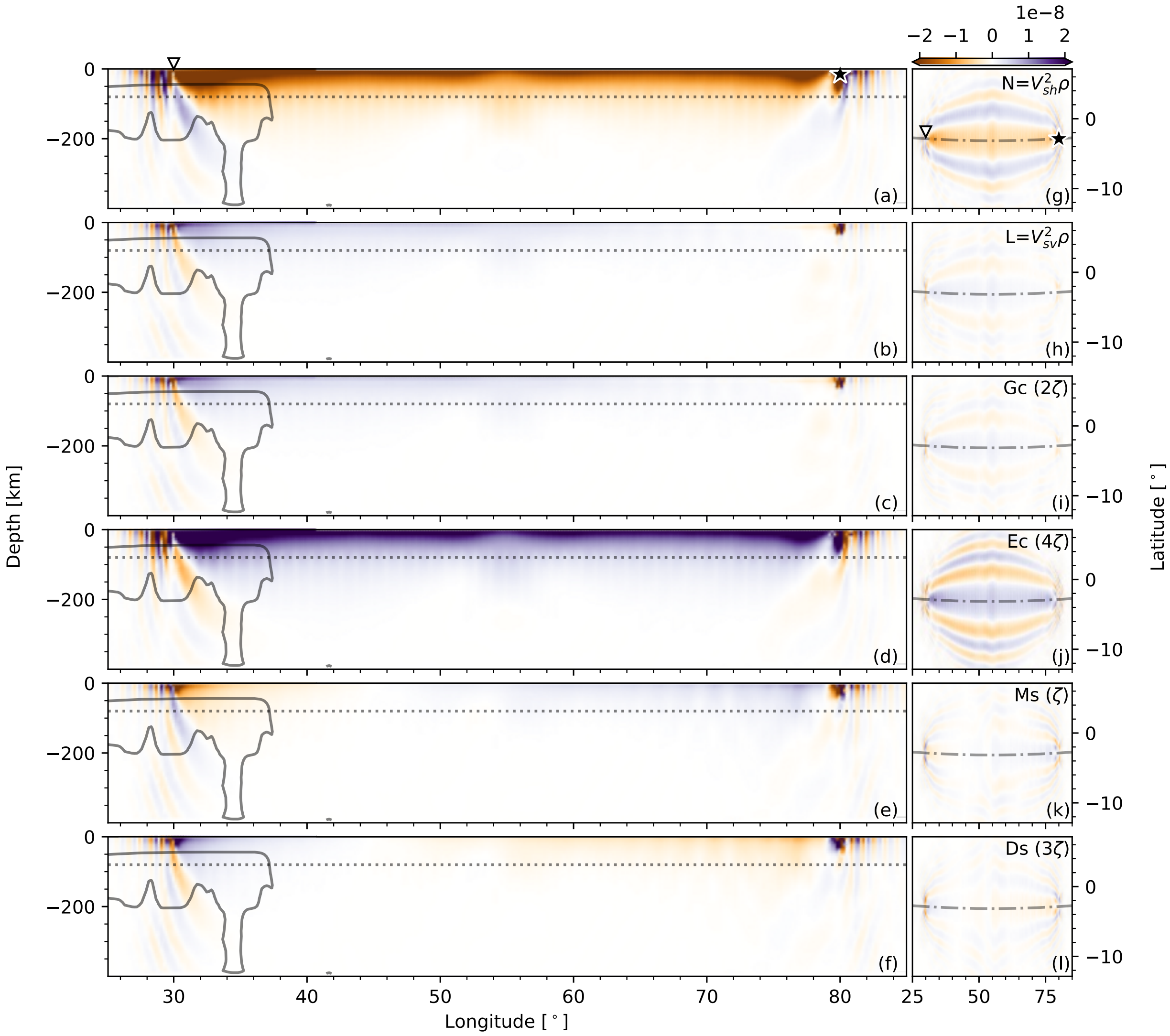

Figure 8. Amplitude kernels of selected parameters for fundamental-mode Love wave measurements made on the North component N, in units GPa^{-1}m^{-3} (Additional parameters are shown in the supplementary material). The dotted lines in panels a-e indicate the depth ($\sim$ 80 km) at which the slices in panels f-j are taken. The dot-dashed lines in the f-j panels indicate the latitude at which the sections in panels a-e are shown, corresponding to the source-receiver plane. The maximum depth shown in the sections is 400 km, and the plume is outlined by contouring the density anomaly at -0.1%.

2007). The high sensitivity at shallow depths to B_c and E_c is also consistent with their effect on horizontally polarized P waves (Sieminski et al. 2007; Chen & Tromp 2007). Love wave propagation depends on the degree-four parameter E_c, instead (Chen & Tromp 2007; Montagner & Nataf 1986; Rappisi et al. 2024): see Fig. 8d.

The parameters $J_{c,s},\ K_{c,s},\ M_{c,s}$ ($\sim \zeta$) and $D_{c,s}$ ($\sim 3\zeta$) control only body wave propagation

(Chen & Tromp 2007, e.g,). Thus, low sensitivity is obtained in the source-receiver plane for all surface-wave measurements (see Figs. 7, S3 and S6). Love waves are slightly more sensitive to M_s and D_s, since these parameters affect the polarization of S waves and S-wave splitting (Sieminski et al. 2007; Chen & Tromp 2007).

For all surface waves, null sensitivity is obtained for $B_s,\ H_s,\ G_s$ and E_s in the source-receiver plane (see, e.g., Figs. 6, S5 and S2) consistent with Eq. 1, given our source-receiver geometry. Similarly, for $J_c,\ K_c,\ M_c$ and D_c, sensitivity is null (see Chen & Tromp 2007).

4.2 Finite-frequency effects

Sensitivities far from the great circle path are not predicted by asymptotic theory, and are due instead to finite-frequency effects (e.g., Sieminski et al. 2007). Namely, self-coupling of the surface-wave fundamental mode is responsible for the elliptical shape of the kernels along the great circle path: see, e.g., Figs.5j, S1j, for Rayleigh-wave self-coupling, and Fig. 8g) for Love-wave self-coupling (Zhou et al. 2011, 2004).

Oscillatory fringes in the kernels further away from the great-circle path are instead due to Love-Rayleigh coupling (Zhou et al. 2004, 2011; Sieminski et al. 2007). Namely, Rayleigh-wave measurements on the vertical (Z) component are sensitive to Love-to-Rayleigh scattering. This manifests as two bands of fringes originating from the source and at $\sim 45°$ angles with respect to the great circle path (see, e.g., Fig. 5h). The geometry of these bands stems from the chosen source mechanism, whose radiation pattern for Love waves has maxima at those angles (see Fig. A2). Secondly, scattered Rayleigh waves cannot reach the receiver within the designated time-window if the perturbations that cause them are imposed at wider angles and/or larger distances from the source. Conversely, Rayleigh-wave measurements on the radial (E) component are also sensitive to Rayleigh-to-Love scattering (given the receiver polarization). This type of coupling manifests as two additional bands originating from the receiver at $\sim 45°$ angles (see, e.g., Fig. S1h). Their placement stems from the chosen radiation pattern for Rayleigh waves, with a maximum towards the receiver. Also, only Love waves scattered relatively near the receiver and at $\sim 45°$ angles can reach it within the designated time-window (the raypaths for Love-to-Rayleigh and Rayleigh-to-Love scattering are reciprocal).

For Rayleigh-wave measurements, most of the kernels exhibit both self- and Love-Rayleigh coupling effects (see, e.g., Fig. 6j), while others are entirely characterized by the latter (see, e.g., Figs. 5h and 6i, l and). In particular, since the propagation of Rayleigh waves should not strongly depend on V_{Sh} (e.g, Chen & Tromp 2007), their sensitivity to N can be only accounted for by this kind of coupling. Similarly, $M_{c,s}$ and $D_{c,s}$ control S-wave polarization angles in the plane orthogonal to the ray path (Chen & Tromp 2007), affecting Rayleigh-wave measurements mainly via Love-Rayleigh scattering (see Sieminski et al. 2007).

Finally, the strength and sign of these coupling effects depend on the scattering angle (Zhou et al. 2004; Zhou & Greenhalgh 2011). Thus, several azimuthal anisotropy kernels are asymmetric (see, e.g., Figs. 6m-p and 7m-p). For a symmetric source radiation pattern, as considered here, this asymmetry in the amplitude (and phase) kernels is uniquely associated with azimuthal anisotropy (Sieminski et al. 2007).

4.3 Comparison with phase kernels

We find that surface-wave amplitude measurements are strongly sensitive to perturbations in the same anisotropic elastic structure that governs phase measurements (see Figs. S7–S15), reflecting the role of these structural variations in focusing and defocusing the seismic wavefield (e.g., Dunn & Forsyth 2003; Dalton & Ekström 2006; Selby & Woodhouse 2000). Importantly, Fig. 9 shows that the spatial patterns of amplitude and phase kernels are 'staggered' relative to each other (Zhou et al. 2011; Dahlen & Baig 2002), implying that these observables are sensitive to complementary Earth structure information. Namely, sensitivities of amplitude measurements are more narrowly focused along the great circle path than for phase measurements. Moreover, the kernels for the two measurement types are shifted in space by roughly a quarter of a wavelength either side from the centre (see, e.g., Fig. 9b). Amplitude and phase measurements have instead a similar pattern of depth sensitivity, aside from for the different order of magnitude (see, e.g., Fig. 9a). Indeed, the main difference between amplitude and phase kernels is in the adjoint source time-functions, which differ by a $\pi/2$ phase from each other (see Equations 4, 5). From a theoretical perspective, Born theory provides a natural connection between phase and amplitude sensitivities: in the frequency domain, the corresponding kernels can be expressed as the imaginary and real parts, respectively, of relative perturbations in the displacement field (Zhou et al. 2004). Our finding that surface-wave amplitudes are strongly sensitive to the same anisotropic parameters as phase measurements is therefore consistent with this fundamental relationship, while demonstrating its implications for sensitivity to the full anisotropic elastic structure.

4.4 Amplitude measurements and anisotropic tomography

An important implication of the results presented above is that amplitude measurements are sensitive to anisotropy and, in tandem with phase measurements, may be used to enhance data coverage by maximizing the amount of information extracted from seismic data (Lekić & Romanowicz 2011; Bozdağ et al. 2011; Fichtner et al. 2024). Indeed, since amplitude measurements are strongly sensitive to small-scale variations in elastic properties, valuable (but generally neglected) information is encoded in the waveform amplitude (Ferreira & Woodhouse 2007; Romanowicz 1987; Dalton & Ekström 2006; Selby & Woodhouse 2000). For instance, ray-based inversions of isotropic phase velocity maps have been performed with amplitude data (alone or together with phase measurements, Selby & Woodhouse 2000; Dalton & Ekström 2006). Critically, ray theory predicts that surface-wave amplitudes depend on the second transverse derivative of phase-velocity variations (e.g., Romanowicz 1987; Woodhouse & Wong 1986; Dalton & Ekström 2006): as shown in this and previous studies, finite-frequency theory instead predicts strong sensitivities up to ~ 700 kms away from the ray (see, e.g. Fig. 5). Future efforts should rigorously test these effects on anisotropic inversions. Enhancing data coverage through the addition of complementary observables is one of the most promising directions for improving the resolution of tomographic images, particularly in anisotropic tomography. Indeed, accounting for anisotropy implies that a higher number of inversion parameters must be considered, adding to the ill-posedness of the inverse problem. On the other hand, an excessively simple parametrization may introduce spurious

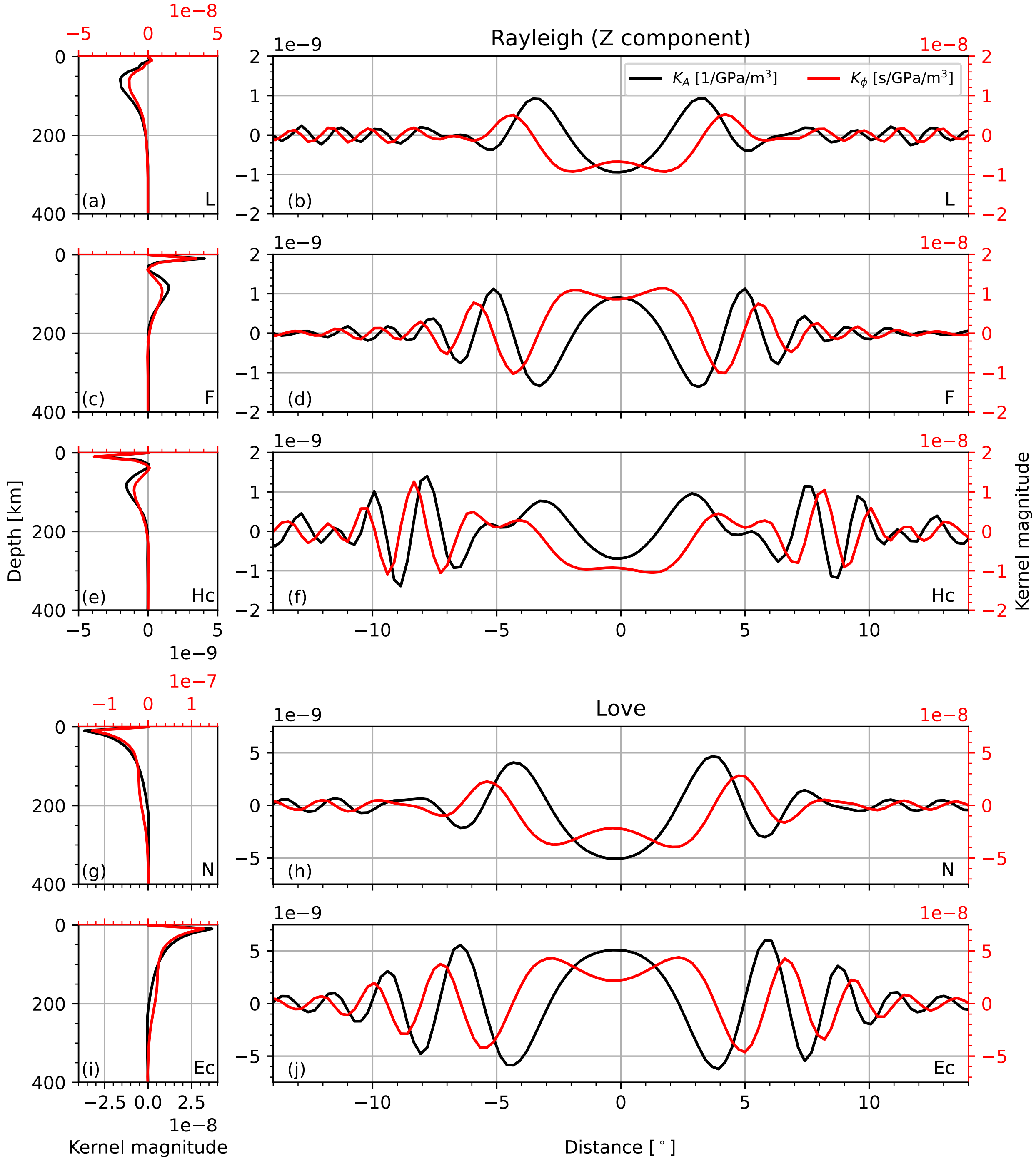

Figure 9. Comparison between amplitude and phase kernels (K_A and K_ϕ), for several example parameters taken from Figs. 5, 6 and 8 (as labelled). Panels a, c, e show depth-profiles, while panels b, d, f show horizontal profiles along latitude, for Rayleigh waves. Depth profiles are taken at the plume location. Horizontal profiles are taken at the source-receiver mid-point, orthogonal to the great circle path, and the horizontal axes shows distance from the centre. The same is shown for Love waves in panels g-j. The period band for this computation is [40, 60] s.

artifacts in the inversion and bias the interpretation (Faccenda & VanderBeek 2023; Rappisi et al. 2024; Fichtner et al. 2024; Del Piccolo et al. 2024).

Disentangling wavefield focusing effects from intrinsic attenuation (Dalton & Ekström 2006; Selby & Woodhouse 2000) may challenge our ability to exploit amplitude measurements in inversions for elastic structure (Fichtner et al. 2024)– and, thus, for anisotropy. However, sensitivity to anelasticity and its effects can be minimized or fully accounted for in tomographic inversions (Selby & Woodhouse 2000; Dalton & Ekström 2006; Zhou 2009). Uncertainties in the source mechanisms may also affect the inversions (Dalton & Ekström 2006). However, this can be overcome by inverting for source mechanisms (either separately or jointly, see e.g., Bozdağ et al. 2016): contrary to ray-based sensitivities, finite-frequency kernels like those shown in this study naturally incorporate the effects of source radiation patterns (e.g., Zhou et al. 2006).

Finally, we stress the importance of computing sensitivities to amplitude and phase measurements separately, as done here, in the context of full-waveform inversions. Indeed, the adjoint-method is ultimately designed for waveform misfit computation in a full-waveform framework (e.g., Tape et al. 2007). Waveform optimization is, however, a highly non-linear problem (Luo & Schuster 1991; Gauthier et al. 1986), which can be mitigated by treating phase and amplitude information separately: for example, via discrete misfit functions– or, equivalently, adjoint sources– for phase and amplitude observables, respectively (Fichtner et al. 2008; Bozdağ et al. 2011).

4.5 Combined measurements

Fundamental observables can be combined to satisfy desirable requirements, such as maximizing the sensitivity near the receiver. To this end, we calculate the difference between kernels for Rayleigh-wave measurements made on the east and vertical component (E and Z). Because of the linearity of the integral in Equation 12, this is equivalent to computing the kernel for the difference of the measurements.

Fig. 10a-f shows the kernel for the difference between E- and Z-component phase-shifts measurements. For these kernels, high sensitivity is generally obtained only within a $300-700$ km horizontal distance within the receiver, and at depths shallower than 190 km (see, e.g., Fig. 10a and d).

Beyond this range, sensitivities decrease by ~ 2 orders of magnitude. Indeed, phase kernels for the two components are similar to each other east of the receiver (compare, e.g., Figs. S7, S8). Thus, taking the difference between the E and Z kernels enhances sensitivity on the receiver side. This is also consistent with non-elliptical particle-motion in an anisotropic medium: instead, the phase between the two components of displacement deviates from $\pi/2$ and depends on local anisotropic structure (e.g., Crampin 1975).

Fig. 10g-l shows the kernel for the difference between relative amplitude variations measured on the E- and Z-component, respectively. In this case, the combined kernel is equivalent to that of the ratio between the Horizontal and Vertical displacement components, or HV ratio (the horizontal component is aligned with the east direction). Indeed, the kernel K_{HV} for the HV ratio is, according to Maupin (2017):

$$K_{HV} = K_{dlnA_H/A_H} - K_{dlnA_V/A_V} \tag{15}$$

where K_{dlnA_*/A_*} are the kernels for relative amplitude variations on the horizontal and vertical component. As phase and amplitude kernels are similar in their broad spatial features, the sensitivity for the combined amplitude observable is also maximized close to and below the receiver (see, e.g., Fig. 10g and j). Moreover, although ellipticity is not well defined in the anisotropic case (Yano et al. 2009; Crampin 1975), these results are similar to those obtained by Maupin (2017) in the isotropic case (wherein the HV ratio measures Rayleigh wave ellipticity exactly).

4.6 Combined measurements and anisotropic tomography

These results suggest that combining phase and amplitude measurements can improve constraints on local elastic structure from regional and teleseismic events, analogous to approaches based on co-located rotational and translational measurements but without the cost and sensitivity limitations of rotational sensors (e.g., Bernauer et al. 2009; Ferreira & Igel 2009; Simonelli et al. 2018). This approach may be particularly valuable for improving lateral resolution in sparsely instrumented regions, such as the ocean floor in ridge and hotspot settings (e.g., Ferreira & UPFLOW team 2026), as well as for single-station analyses in planetary seismology (Banerdt et al. 2020).

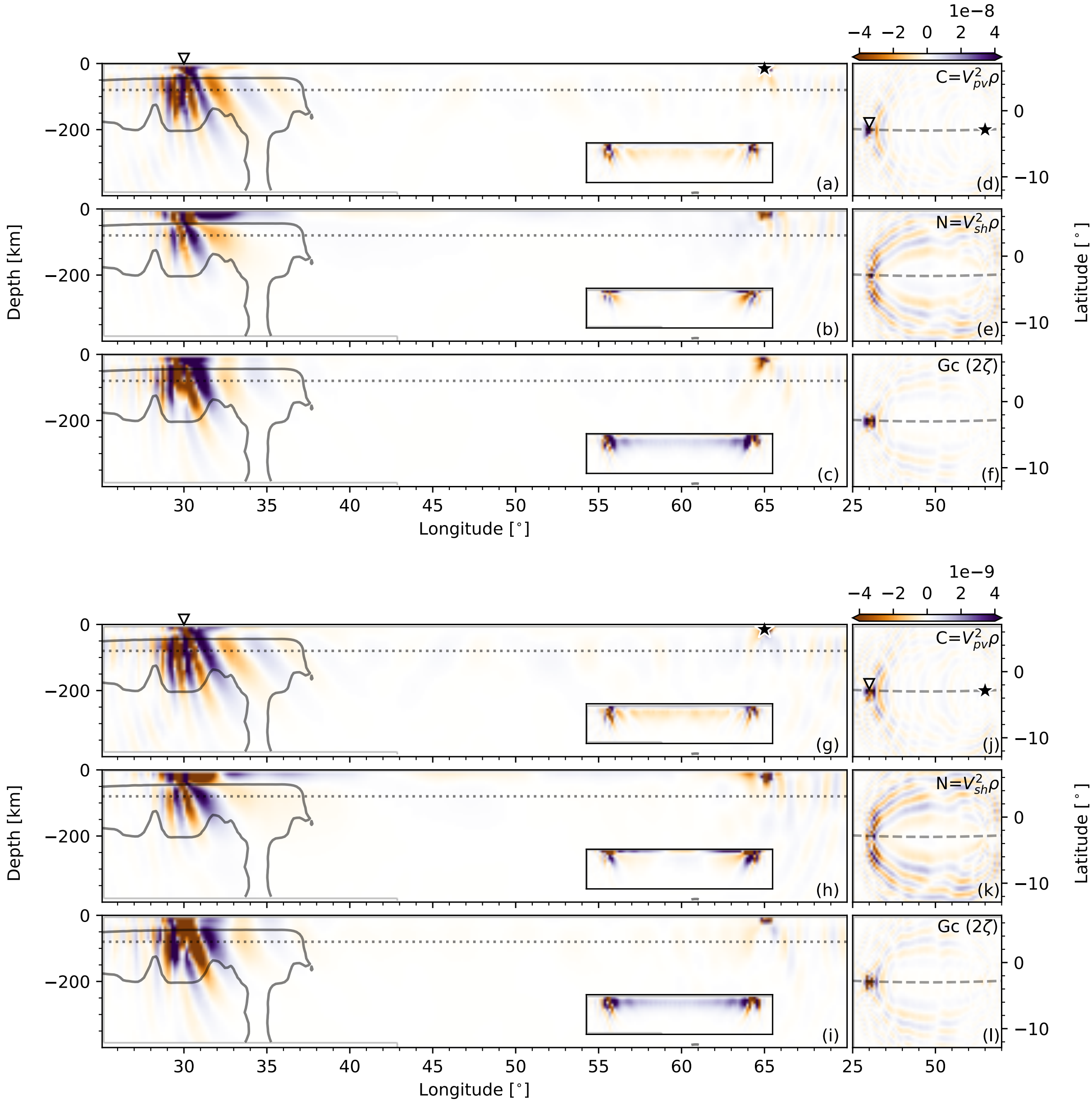

Figure 10. Kernels for combined fundamental-mode Rayleigh-wave measurements. Panels a-f: Kernels of differences between phase measurements made on the E and Z components, in units s GPa^{-1}m^{-3}; Panels g-l: kernels of differences between relative amplitude variations measurements made on the E and Z components– corresponding to HV-ratio kernels– in units GPa^{-1}m^{-3}. Kernels for E-component measurements are displayed in the insets for reference, showing that the combined measurements generally maximize the sensitivity close to the receiver. The full kernel galleries are collected in Figs. S16–S21). All other details are as in Fig. 5.

Its application to anisotropic tomographic inversions warrants further investigation, including the effects of noise and inter-parameter tradeoffs.

A limitation is that combined measurements do not consistently suppress far-field sensitivity for all parameters. For N, E_c, M_c, and M_s, appreciable sensitivity persists at ~ 700 km from the great-circle path. This results from differences in mode-coupling sensitivity between the Z and E components: the Z component is primarily sensitive to Love–Rayleigh coupling near the source, whereas the E component is also sensitive to Rayleigh–Love coupling near the receiver. Consequently, differencing the corresponding kernels enhances the contrast between the two halves of the sensitivity pattern. These effects may, however, be reduced through appropriate time-window selection (Sieminski et al. 2007). Optimal observable design (Bernauer et al. 2014) provides a promising avenue for further testing and exploiting these localized sensitivities, including reducing inter-parameter tradeoffs and residual far-field sensitivity. These applications are beyond the scope of the present study.

5 CONCLUSIONS

In this study, we presented amplitude kernels for fundamental-mode Love and Rayleigh waves, computed for the first time with respect to variations in all the 21 independent elastic constants that control full seismic anisotropy in the Earth. Differently from previous analogous studies, we applied mineral fabrics calculations to a 3D geodynamic model of a realistic upper-mantle plume setting, and used that as a physically self-consistent, anisotropic background medium for our kernel computations. These are carried out using the adjoint method, thus fully modelling 3D finite-frequency effects on sensitivity. A key finding is that amplitude measurements are strongly sensitive to the same anisotropy parameters as phase measurements. Importantly, amplitude kernels are laterally shifted compared to phase kernels, outward from the central axis of simmetry (i.e., the direct ray path). An important implication of this is that amplitudes encode complementary information on anisotropic Earth structure compared to phase measurements, with implications for improving the robustness of upper mantle anisotropy tomographic inversions. Another key finding is that sensitivity to anisotropic structure near and below the receiver is maximised by combining kernels for measurements made using different receiver components, both for amplitudes and phase. Our results highlight the potential of applying observables beyond phase measurements and travel times to augment the resolution of anisotropic tomography inversions and, in turn, enhance our understanding of mantle dynamics.

ACKNOWLEDGMENTS

M.D., A.M.G.F. and S.P.H. are grateful for the support from the ERC Horizon Fund (UPFLOW project; grant agreement 101001601). S.P.H. is also grateful for funding from a NERC Independent Research Fellowship (UKRI184; NE/B000184/1). F.R. acknowledges the support of the European Center for Geodynamics and Seismology (ECGS) through internal institutional funds. M.F. acknowledges the ERC Horizon Fund (NEWTON project; grant agreement 758199). A.M.C.C. and M.D.B. have been supported by UK Research and Innovation under NERC grant NE/X000508/1. The authors acknowledge the use of the UCL Myriad High Performance Computing Facility (Myriad@UCL), and associated support services, in the completion of this work. The authors declare that they have no conflict of interest.

DATA AVAILABILITY

The version of the code SPECFEM3D_GLOBE used in this study, as well as the geodynamic input model, the result of the D-REX post-processing, the kernels and the parameter file used for the adjoint simulations can be downloaded from two online repositories (Rappisi et al. 2026; Desiderio et al. 2026). Figures were created with Matplotlib, PyVista and GMT (Hunter 2007; Sullivan & Kaszynski 2019; Wessel et al. 2026).

REFERENCES

Anderson, D. L., 1965. Recent evidence concerning the structure and composition of the Earth's mantle, *Physics and Chemistry of the Earth*, doi: 10.1016/0079-1946(65)90013-3.

Ballmer, M. D., Van Hunen, J., Ito, G., Bianco, T. A., & Tackley, P. J., 2009. Intraplate volcanism with complex age-distance patterns: A case for small-scale sublithospheric convection, *Geochemistry, Geophysics, Geosystems*, **10**(6), 2009GC002386, doi: 10.1029/2009GC002386.

Banerdt, W. B., Smrekar, S. E., Banfield, D., Giardini, D., Golombek, M., Johnson, C. L., Lognonné, P., Spiga, A., Spohn, T., Perrin, C., Stähler, S. C., Antonangeli, D., Asmar, S., Beghein, C., Bowles, N., Bozdag, E., Chi, P., Christensen, U., Clinton, J., Collins, G. S., Daubar, I., Dehant, V., Drilleau, M., Fillingim, M., Folkner, W., Garcia, R. F., Garvin, J., Grant, J., Grott, M., Grygorczuk, J., Hudson, T., Irving, J. C. E., Kargl, G., Kawamura, T., Kedar, S., King, S., Knapmeyer-Endrun, B., Knapmeyer, M., Lemmon, M., Lorenz, R., Maki, J. N., Margerin, L., McLennan, S. M., Michaut, C., Mimoun, D., Mittelholz, A., Mocquet, A., Morgan, P., Mueller, N. T., Murdoch, N., Nagihara, S., Newman, C., Nimmo, F., Panning, M., Pike, W. T., Plesa, A.-C., Rodriguez, S., Rodriguez-Manfredi, J. A., Russell, C. T., Schmerr, N., Siegler, M., Stanley, S., Stutzmann, E., Teanby, N., Tromp, J., van Driel, M., Warner, N., Weber, R., & Wieczorek, M., 2020. Initial results from the InSight mission on Mars, *Nature Geoscience*, **13**(3), 183–189, doi: 10.1038/s41561-020-0544-y.

Bernauer, M., Fichtner, A., & Igel, H., 2009. Inferring earth structure from combined measurements of rotational and translational ground motions, *Geophysics*, **74**(6), WCD41–WCD47, doi: 10.1190/1.3211110.

Bernauer, M., Fichtner, A., & Igel, H., 2014. Optimal observables for multiparameter seismic tomography, *Geophysical Journal International*, **198**(2), 1241–1254, doi: 10.1093/gji/ggu204.

Boneh, Y., Morales, L. F. G., Kaminski, E., & Skemer, P., 2015. Modeling olivine CPO evolution with complex deformation histories: Implications for the interpretation of seismic anisotropy in the mantle, *Geochemistry, Geophysics, Geosystems*, **16**(10), 3436–3455, doi: 10.1002/2015GC005964, _eprint: https://agupubs.onlinelibrary.wiley.com/doi/pdf/10.1002/2015GC005964.

Bozdağ, E., Trampert, J., & Tromp, J., 2011. Misfit functions for full waveform inversion based on instantaneous phase and envelope measurements, *Geophysical Journal International*, **185**(2), 845–870, doi: 10.1111/j.1365-246X.2011.04970.x.

Bozdağ, E., Peter, D., Lefebvre, M., Komatitsch, D., Tromp, J., Hill, J., Podhorszki, N., & Pugmire, D., 2016. Global adjoint tomography: first-generation model, *Geophysical Journal International*, **207**(3), 1739–1766, doi: 10.1093/gji/ggw356.

Chang, S.-J., Ferreira, A. M. G., Ritsema, J., van Heijst, H. J., & Woodhouse, J. H., 2014. Global radially anisotropic mantle structure from multiple datasets: A review, current challenges, and outlook, *Tectonophysics*, **617**, 1–19, doi: 10.1016/j.tecto.2014.01.033.

Chang, S.-J., Ferreira, A. M. G., Ritsema, J., van Heijst, H. J., & Woodhouse, J. H., 2015. Joint inversion for global isotropic and radially anisotropic mantle structure including crustal thickness perturbations, *Journal of Geophysical Research: Solid Earth*, **120**(6), 4278–4300, doi: 10.1002/2014JB011824, _eprint: https://onlinelibrary.wiley.com/doi/pdf/10.1002/2014JB011824.

Chen, M. & Tromp, J., 2007. Theoretical and numerical investigations of global and regional seismic wave propagation in weakly anisotropic earth models, *Geophysical Journal International*, **168**(3), 1130–1152, doi: 10.1111/j.1365-246X.2006.03218.x.

Christensen, U. R. & Yuen, D. A., 1985. Layered convection induced by phase transitions, *Journal of Geophysical Research: Solid Earth*, **90**(B12), 10291–10300, doi: 10.1029/JB090iB12p10291, _eprint: https://onlinelibrary.wiley.com/doi/pdf/10.1029/JB090iB12p10291.

Chust, T. C., Steinle-Neumann, G., Dolejš, D., Schuberth, B. S. A., & Bunge, H.-P., 2017. MMA-EoS: A Computational Framework for Mineralogical Thermodynamics, *Journal of Geophysical Research: Solid Earth*, **122**(12), 9881–9920, doi: 10.1002/2017JB014501, _eprint: https://agupubs.onlinelibrary.wiley.com/doi/pdf/10.1002/2017JB014501.

Crampin, S., 1975. Distinctive Particle Motion of Surface Waves as a Diagnostic of Anisotropic Layering, *Geophysical Journal International*, **40**(2), 177–186, doi: 10.1111/j.1365-246X.1975.tb07045.x.

Dahlen, F. A. & Baig, A. M., 2002. Fréchet kernels for body-wave amplitudes, *Geophysical Journal International*, **150**(2), 440–466, doi: 10.1046/j.1365-246X.2002.01718.x.

Dahlen, F. A., Hung, S.-H., & Nolet, G., 2000. Fréchet kernels for finite-frequency traveltimes—I. Theory, *Geophysical Journal International*, **141**(1), 157–174, doi: 10.1046/j.1365-246X.2000.00070.x.

Dalton, C. A. & Ekström, G., 2006. Constraints on global maps of phase velocity from surface-wave amplitudes, *Geophysical Journal International*, **167**(2), 820–826, doi: 10.1111/j.1365-246X.2006.03142.x.

Dalton, C. A., Hjörleifsdóttir, V., & Ekström, G., 2014. A comparison of approaches to the prediction of surface wave amplitude, *Geophysical Journal International*, **196**(1), 386–404, doi: 10.1093/gji/ggt365.

Debayle, E. & Kennett, B., 2000. Anisotropy in the Australasian upper mantle from Love and Rayleigh waveform inversion, *Earth and Planetary Science Letters*, **184**(1), 339–351, doi: 10.1016/S0012-821X(00)00314-9.

Debayle, E., Dubuffet, F., & Durand, S., 2016. An automatically updated S-wave model of the upper mantle and the depth extent of azimuthal anisotropy, *Geophysical Research Letters*, **43**(2), 674–682, doi: 10.1002/2015GL067329, _eprint: https://agupubs.onlinelibrary.wiley.com/doi/pdf/10.1002/2015GL067329.

Del Piccolo, G., VanderBeek, B. P., Faccenda, M., Morelli, A., & Byrnes, J. S., 2024. Imaging Upper-Mantle Anisotropy with Transdimensional Bayesian Monte Carlo Sampling, *Bulletin of the Seismological Society of America*, **114**(3), 1214–1226, doi: 10.1785/0120230233.

Desiderio, M., Faccenda, M., Ferreira, A. M. G., Manjón-Cabeza Córdoba, A., Rappisi, F., Hicks, S., & Ballmer, M. D., 2026. Anisotropic seismo-geodynamic input model for adjoint sensitivity computations in SPECFEM3D_globe and kernels, doi: 10.5281/zenodo.21240210.

Dunn, R. A. & Forsyth, D. W., 2003. Imaging the transition between the region of mantle melt generation and the crustal magma chamber beneath the southern East Pacific Rise with short-period Love waves, *Journal of Geophysical Research: Solid Earth*, **108**(B7), doi: 10.1029/2002JB002217, _eprint: https://agupubs.onlinelibrary.wiley.com/doi/pdf/10.1029/2002JB002217.

Dziewonski, A. M. & Anderson, D. L., 1981. Preliminary reference Earth model, *Physics of the Earth and Planetary Interiors*, **25**(4), 297–356, doi: 10.1016/0031-9201(81)90046-7.

Faccenda, M. & VanderBeek, B. P., 2023. On constraining 3D seismic anisotropy in subduction, mid-ocean-ridge, and plume environments with teleseismic body wave data, *Journal of Geodynamics*, **158**, 102003, doi: 10.1016/j.jog.2023.102003.

Faccenda, M., VanderBeek, B. P., de Montserrat, A., Yang, J., Rappisi, F., & Ribe, N., 2024. ECOMAN: an open-source package for geodynamic and seismological modelling of mechanical anisotropy, *Solid Earth*, **15**(10), 1241–1264, doi: 10.5194/se-15-1241-2024.

Ferreira, A. M. G. & Igel, H., 2009. Rotational Motions of Seismic Surface Waves in a Laterally Heterogeneous Earth, *Bulletin of the Seismological Society of America*, **99**(2B), 1429–1436, doi: 10.1785/0120080149.

Ferreira, A. M. G. & UPFLOW team, 2026. Charting the mantle, *Astronomy & Geophysics*, **67**(2), 2.35–2.40, doi: 10.1093/astrogeo/atag007.

Ferreira, A. M. G. & Woodhouse, J. H., 2007. Source, path and receiver effects on seismic surface waves, *Geophysical Journal International*, **168**(1), 109–132, doi: 10.1111/j.1365-246X.2006.03092.x.

Fichtner, A., Kennett, B. L. N., Igel, H., & Bunge, H.-P., 2008. Theoretical background for continental- and global-scale full-waveform inversion in the time-frequency domain, *Geophysical Journal International*, **175**(2), 665–685, doi: 10.1111/j.1365-246X.2008.03923.x.

Fichtner, A., Kennett, B. L. N., Tsai, V. C., Thurber, C. H., Rodgers, A. J., Tape, C., Rawlinson, N., Borcherdt, R. D., Lebedev, S., Priestley, K., Morency, C., Bozdağ, E., Tromp, J., Ritsema, J., Romanowicz, B., Liu, Q., Golos, E., & Lin, F., 2024. Seismic Tomography 2024, *Bulletin of the Seismological Society of America*, **114**(3), 1185–1213, doi: 10.1785/0120230229.

Foley, B. J. & Driscoll, P. E., 2016. Whole planet coupling between climate, mantle, and core: Implications for rocky planet evolution, *Geochemistry, Geophysics, Geosystems*, **17**(5), 1885–1914, doi: 10.1002/2015GC006210, _eprint: https://agupubs.onlinelibrary.wiley.com/doi/pdf/10.1002/2015GC006210.

Gauthier, O., Virieux, J., & Tarantola, A., 1986. Two-dimensional nonlinear inversion of seismic waveforms; numerical results, *Geophysics*, **51**(7), 1387–1403, doi: 10.1190/1.1442188.

Gung, Y., Panning, M., & Romanowicz, B., 2003. Global anisotropy and the thickness of continents, *Nature*, **422**(6933), 707–711, doi: 10.1038/nature01559.

Heintz, M., Debayle, E., & Vauchez, A., 2005. Upper mantle structure of the South American continent and neighboring oceans from surface wave tomography, *Tectonophysics*, **406**(1-2), 115–139, doi: 10.1016/j.tecto.2005.05.006.

Hung, S.-H., Dahlen, F., & Nolet, G., 2000. Fréchet kernels for finite-frequency traveltimes II. Examples, *Geophysical Journal International*, **141**(1), 175–203, doi: 10.1046/j.1365-246X.2000.00072.x.

Hunter, J. D., 2007. Matplotlib: A 2D graphics environment, *Computing in Science & Engineering*, **9**(3), 90–95, doi: 10.1109/MCSE.2007.55.

Kaminski, E., Ribe, N. M., & Browaeys, J. T., 2004. D-Rex, a program for calculation of seismic anisotropy due to crystal lattice preferred orientation in the convective upper mantle, *Geophysical Journal International*, **158**(2), 744–752, doi: 10.1111/j.1365-246X.2004.02308.x.

Karato, S.-i., Jung, H., Katayama, I., & Skemer, P., 2008. Geodynamic Significance of Seismic Anisotropy of the Upper Mantle: New Insights from Laboratory Studies, *Annual Review of Earth and Planetary Sciences*, **36**(1), 59–95, doi: 10.1146/annurev.earth.36.031207.124120.

Komatitsch, D., 2010. Fluid–solid coupling on a cluster of GPU graphics cards for seismic wave propagation, *Comptes Rendus. Mécanique*, **339**(2-3), 125–135, doi: 10.1016/j.crme.2010.11.007.

Komatitsch, D. & Tromp, J., 2002. Spectral-element simulations of global seismic wave propagation-I. Validation, *Geophysical Journal International*, **149**(2), 390–412, doi: 10.1046/j.1365-246X.2002.01653.x.

Komatitsch, D., Xie, Z., Bozdağ, E., Sales De Andrade, E., Peter, D., Liu, Q., & Tromp, J., 2016. Anelastic sensitivity kernels with parsimonious storage for adjoint tomography and full waveform inversion, *Geophysical Journal International*, **206**(3), 1467–1478, doi: 10.1093/gji/ggw224.

Larson, E., Tromp, J., & Ekström, G., 1998. Effects of slight anisotropy on surface waves, *Geophysical Journal International*, **132**(3), 654–666, doi: 10.1046/j.1365-246X.1998.00452.x.

Laske, G., Markee, A., Orcutt, J. A., Wolfe, C. J., Collins, J. A., Solomon, S. C., Detrick, R. S., Bercovici, D., & Hauri, E. H., 2011. Asymmetric shallow mantle structure beneath the Hawaiian Swell-evidence from Rayleigh waves recorded by the PLUME network: Shallow mantle structure of the Hawaiian swell, *Geophysical Journal International*, **187**(3), 1725–1742, doi: 10.1111/j.1365-246X.2011.05238.x.

Lekić, V. & Romanowicz, B., 2011. Inferring upper-mantle structure by full waveform tomography with the spectral element method: SEM based global tomography, *Geophysical Journal International*, **185**(2), 799–831, doi: 10.1111/j.1365-246X.2011.04969.x.

Li, X.-D. & Romanowicz, B., 1995. Comparison of global waveform inversions with and without considering cross-branch modal coupling, *Geophysical Journal International*, **121**(3), 695–709, doi: 10.1111/j.1365-246X.1995.tb06432.x.

Liu, Q. & Tromp, J., 2008. Finite-frequency sensitivity kernels for global seismic wave propagation based upon adjoint methods, *Geophysical Journal International*, **174**(1), 265–286, doi: 10.1111/j.1365-246X.2008.03798.x, _eprint: https://onlinelibrary.wiley.com/doi/pdf/10.1111/j.1365-246X.2008.03798.x.

Love, A. E. H., 1911. *Some problems of geodynamics*, Cambridge University Press.

Luo, Y. & Schuster, G. T., 1991. Wave equation inversion of skeletalized geophysical data, *Geophysical Journal International*, **105**(2), 289–294, doi: 10.1111/j.1365-246X.1991.tb06713.x.

Manjón-Cabeza Córdoba, A. & Ballmer, M. D., 2022. The role of edge-driven convection in the generation of volcanism – Part 2: Interaction with mantle plumes, applied to the Canary Islands, *Solid Earth*, **13**(10), 1585–1605, doi: 10.5194/se-13-1585-2022.

Mathar, J. P., Ritter, J. R. R., & Friederich, W., 2006. Surface waves image the top of the Eifel plume, *Geophysical Journal International*, **164**(2), 377–382, doi: 10.1111/j.1365-246X.2006.02835.x.

Maupin, V., 2017. 3-D sensitivity kernels of the Rayleigh wave ellipticity, *Geophysical Journal International*, **211**(1), 107–119, doi: 10.1093/gji/ggx294.

Montagner, J.-P. & Nataf, H.-C., 1986. A simple method for inverting the azimuthal anisotropy of surface waves, *Journal of Geophysical Research: Solid Earth*, **91**(B1), 511–520, doi: 10.1029/JB091iB01p00511, _eprint: https://agupubs.onlinelibrary.wiley.com/doi/pdf/10.1029/JB091iB01p00511.

Montagner, J.-P. & Tanimoto, T., 1991. Global upper mantle tomography of seismic velocities and anisotropies, *Journal of Geophysical Research: Solid Earth*, **96**(B12), 20337–20351, doi: 10.1029/91JB01890, _eprint: https://agupubs.onlinelibrary.wiley.com/doi/pdf/10.1029/91JB01890.

Moresi, L.-N. & Solomatov, V. S., 1995. Numerical investigation of 2D convection with extremely large viscosity variations, *Physics of Fluids*, **7**(9), 2154–2162, doi: 10.1063/1.868465.

Rappisi, F., Witek, M., Faccenda, M., Ferreira, A. M. G., & Chang, S. J., 2024. Artificial age-independent seismic anisotropy, slab thickening and shallowing due to limited resolving power of (an)isotropic tomography, *Geophysical Journal International*, **237**(1), 217–234, doi: 10.1093/gji/ggae042.

Rappisi, F., Faccenda, M., Witek, M., Chang, S.-J., & Ferreira, A. M., 2026. SubRidge: a Subduction-to-Ridge Model with Synthetic Seismic Waveforms for Benchmarking, *Seismica*, **5**(1), doi: 10.26443/seismica.v5i1.2056.

Ritsema, J., Deuss, A., Van Heijst, H., & Woodhouse, J., 2011. S40RTS: a degree-40 shear-velocity model for the mantle from new Rayleigh wave dispersion, teleseismic traveltime and normal-mode splitting function measurements, *Geophysical Journal International*, **184**(3), 1223–1236.

Romanowicz, B., 1987. Multiplet-multiplet coupling due to lateral heterogeneity: asymptotic effects on the amplitude and frequency of the Earth's normal modes, *Geophysical Journal International*, **90**(1), 75–100, doi: 10.1111/j.1365-246X.1987.tb00676.x.

Sebai, A., Stutzmann, E., Montagner, J.-P., Sicilia, D., & Beucler, E., 2006. Anisotropic structure of the African upper mantle from Rayleigh and Love wave tomography, *Physics of the Earth and Planetary Interiors*, **155**(1-2), 48–62, doi: 10.1016/j.pepi.2005.09.009.

Selby, N. D. & Woodhouse, J. H., 2000. Controls on Rayleigh wave amplitudes: attenuation and focusing, *Geophysical Journal International*, **142**(3), 933–940, doi: 10.1046/j.1365-246x.2000.00209.x.

Sieminski, A., Liu, Q., Trampert, J., & Tromp, J., 2007. Finite-frequency sensitivity of surface waves to anisotropy based upon adjoint methods, *Geophysical Journal International*, **168**(3), 1153–1174, doi: 10.1111/j.1365-246X.2006.03261.x.

Sieminski, A., Trampert, J., & Tromp, J., 2009. Principal component analysis of anisotropic finite-frequency sensitivity kernels, *Geophysical Journal International*, **179**(2), 1186–1198, doi: 10.1111/j.1365-246X.2009.04341.x.

Simonelli, A., Igel, H., Wassermann, J., Belfi, J., Di Virgilio, A., Beverini, N., De Luca, G., & Saccorotti, G., 2018. Rotational motions from the 2016, Central Italy seismic sequence, as observed by an underground ring laser gyroscope, *Geophysical Journal International*, **214**(1), 705–715, doi: 10.1093/gji/ggy186.

Smith, M. L. & Dahlen, F. A., 1973. The azimuthal dependence of Love and Rayleigh wave propagation in a slightly anisotropic medium, *Journal of Geophysical Research*, **78**(17), 3321–3333, doi: 10.1029/JB078i017p03321.

Song, T.-R. A. & Kawakatsu, H., 2012. Subduction of oceanic asthenosphere: Evidence from sub-slab seismic anisotropy, *Geophysical Research Letters*, **39**(17), doi: 10.1029/2012GL052639, _eprint: https://agupubs.onlinelibrary.wiley.com/doi/pdf/10.1029/2012GL052639.

Sullivan, C. B. & Kaszynski, A. A., 2019. PyVista: 3D plotting and mesh analysis through a streamlined interface for the Visualization Toolkit (VTK), *Journal of Open Source Software*, **4**(37), 1450, doi: 10.21105/joss.01450.

Tape, C., Liu, Q., & Tromp, J., 2007. Finite-frequency tomography using adjoint methods-Methodology and examples using membrane surface waves, *Geophysical Journal International*, **168**(3), 1105–1129, doi: 10.1111/j.1365-246X.2006.03191.x.

Thrastarson, S., van Herwaarden, D., Noe, S., Josef Schiller, C., & Fichtner, A., 2024. REVEAL: A Global Full-Waveform Inversion Model, *Bulletin of the Seismological Society of America*, **114**(3), 1392–1406, doi: 10.1785/0120230273.

Tromp, J., Tape, C., & Liu, Q., 2005. Seismic tomography, adjoint methods, time reversal and banana-doughnut kernels, *Geophysical Journal International*, **160**(1), 195–216, doi: 10.1111/j.1365-246X.2004.02453.x.

Tromp, J., Komatitsch, D., & Liu, Q., 2008. Spectral-element and adjoint methods in seismology, *Communications in Computational Physics*, **3**(1), 1–32.

Wessel, P., Luis, J. F., Uieda, L., Scharroo, R., Wobbe, F., Smith, W. H. F., Tian, D., Jones, M., & Esteban, F., 2026. The Generic Mapping Tools version 6.7.0, doi: 10.5281/zenodo.19398868.

Woodhouse, J. H. & Dziewonski, A. M., 1984. Mapping the upper mantle: Three-dimensional modeling of earth structure by inversion of seismic waveforms, *Journal of Geophysical Research: Solid Earth*, **89**(B7), 5953–5986, doi: 10.1029/JB089iB07p05953, _eprint:

https://agupubs.onlinelibrary.wiley.com/doi/pdf/10.1029/JB089iB07p05953.

Woodhouse, J. H. & Wong, Y. K., 1986. Amplitude, phase and path anomalies of mantle waves, *Geophysical Journal of the Royal Astronomical Society*, **87**(3), 753–773, doi: 10.1111/j.1365-246X.1986.tb01970.x, _eprint: https://onlinelibrary.wiley.com/doi/pdf/10.1111/j.1365-246X.1986.tb01970.x.

Yano, T., Tanimoto, T., & Rivera, L., 2009. The ZH ratio method for long-period seismic data: inversion for S-wave velocity structure, *Geophysical Journal International*, **179**(1), 413–424, doi: 10.1111/j.1365-246X.2009.04293.x.

Ye, C., Liu, X., Zhao, D., & Zhao, S., 2022. Robust Seismic Images of the Hawaiian Plume, *Geophysical Research Letters*, **49**(23), e2022GL100707, doi: 10.1029/2022GL100707, _eprint: https://agupubs.onlinelibrary.wiley.com/doi/pdf/10.1029/2022GL100707.

Zhou, B. & Greenhalgh, S. A., 2011. Computing the Sensitivity Kernels for 2.5-D Seismic Waveform Inversion in Heterogeneous, Anisotropic Media, *Pure and Applied Geophysics*, **168**(10), 1729–1748, doi: 10.1007/s00024-010-0191-0.

Zhou, Y., 2009. Surface-wave sensitivity to 3-D anelasticity, *Geophysical Journal International*, **178**(3), 1403–1410, doi: 10.1111/j.1365-246X.2009.04230.x, _eprint: https://onlinelibrary.wiley.com/doi/pdf/10.1111/j.1365-246X.2009.04230.x.

Zhou, Y., Dahlen, F. A., & Nolet, G., 2004. Three-dimensional sensitivity kernels for surface wave observables, *Geophysical Journal International*, **158**(1), 142–168, doi: 10.1111/j.1365-246X.2004.02324.x.

Zhou, Y., Dahlen, F. A., Nolet, G., & Laske, G., 2005. Finite-frequency effects in global surface-wave tomography, *Geophysical Journal International*, **163**(3), 1087–1111, doi: 10.1111/j.1365-246X.2005.02780.x, _eprint: https://onlinelibrary.wiley.com/doi/pdf/10.1111/j.1365-246X.2005.02780.x.

Zhou, Y., Nolet, G., Dahlen, F. A., & Laske, G., 2006. Global upper-mantle structure from finite-frequency surface-wave tomography, *Journal of Geophysical Research: Solid Earth*, **111**(B4), doi: 10.1029/2005JB003677, _eprint: https://agupubs.onlinelibrary.wiley.com/doi/pdf/10.1029/2005JB003677.

Zhou, Y., Liu, Q., & Tromp, J., 2011. Surface wave sensitivity: mode summation versus adjoint SEM: Surface wave sensitivity: mode vs adjoint SEM, *Geophysical Journal International*, **187**(3), 1560–1576, doi: 10.1111/j.1365-246x.2011.05212.x.

Zhu, H., Bozdağ, E., Peter, D., & Tromp, J., 2012. Structure of the European upper mantle revealed by adjoint tomography, *Nature Geoscience*, **5**(7), 493–498, doi: 10.1038/ngeo1501.

APPENDIX A: GEODYNAMIC MODEL

We here report the governing equations for the geodynamic model used in this study (Manjón-Cabeza Córdoba & Ballmer 2022). The conservation of mass, momentum and energy are solved in the extended Boussinesq approximation (Christensen & Yuen 1985), although a linear temperature gradient γ is imposed:

$$\nabla \cdot \mathbf{v} = 0 \tag{A.1}$$

$$\nabla[\eta(\nabla \mathbf{v} + \nabla^T \mathbf{v})] - \nabla P = -(RaT + RbF - Rc\phi)\hat{z} \tag{A.2}$$

$$\partial_t T + \mathbf{v} \cdot \nabla T = \nabla^2 T + L(\partial_t F + \mathbf{v} \cdot \nabla F) + DiRa^{-1}\eta\dot{\epsilon}^2 + \gamma v_z \tag{A.3}$$

where $\mathbf{v}$, η, P, T, F, ϕ denote velocity, viscosity, pressure, temperature, depletion of solid residue and melt fraction; Ra, Rb, Rc and Di the thermal, depletion, melt retention Rayleigh numbers and dissipation number (Ballmer et al. 2009); L, $\dot{\epsilon}$ the latent heat, the strain-rate; v_z, $\hat{z}$ the vertical component of the velocity and vertical unit vector. The equations are solved numerically with CitcomCU (Moresi & Solomatov 1995), with modifications described in Ballmer et al. (2009).

APPENDIX B: WAVEFORM SIMULATION - ADDITIONAL INFORMATION

Fig. A1 shows the displacement traces and the adjoint source time-functions derived from those, for amplitude and phase kernel calculations. The traces are shown in the different period bands (a Butterworth filter is used to process the signal). The number of spectral elements along latitude and longitude are $N_{lon} = 160$, $N_{lat} = 144$: hence, the waveform simulations are accurate down to a period $T \simeq (256/N_{lon}) \times (\Delta_{lon}/90) \times 17$ s ~ 30 s, where $\Delta_{lon} = 90°$ is the domain size along longitude (Komatitsch & Tromp 2002).

Fig. A2 shows a schematic map view of the computational setup for the adjoint simulations, for both Love and Rayleigh-wave kernel calculations. Before interpolation on the SPECFEM3D_GLOBE mesh, the DREX model is adapted to the size of the spectral element mesh as follows:

(i) Outside of its boundaries (see box in Fig. A2), the DREX model is extended along latitudes first and longitude second, to fill the size of the mesh.

(ii) A 1D average depth-profile of the model is calculated.

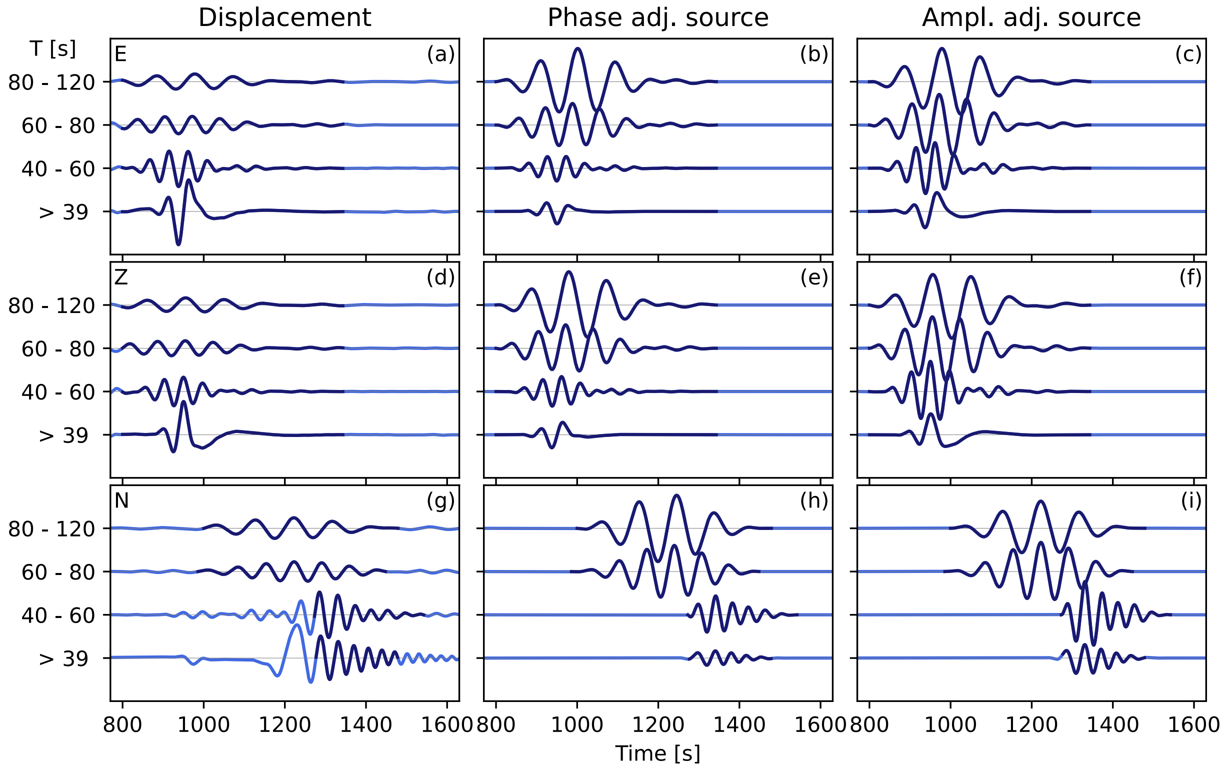

Figure A1. Displacement traces and adjoint-sources calculated for phase and amplitude kernels. The traces are shown in different period bands, as labelled. In this plot, each trace is normalised with respect to its peak value. Panels a-f are centred on the fundamental mode Rayleigh wave arrival. Panels g-i are centred on the fundamental mode Love wave arrival. The time-windows are highlighted in dark.

(iii) Outside of the original DREX boundaries, a smooth transition is applied between the extended model of step 1 and the 1D average.

APPENDIX C: ELASTIC CONSTANTS

In Table A1, we list asymptotic parameters expressed as function of the components of the elastic tensor (as found e.g. in Sieminski et al. 2007). Indexing follows Voigt's convention.

This paper has been produced using the Blackwell Scientific Publications GJI LaTeX2e class file.

Asymptotic parameter	Elastic coefficients
(Degree 0)	
A	$\frac{1}{8}(3C_{11}+3C_{22}+2C_{12}+4C_{66})$
C	C_{33}
N	$\frac{1}{8}(C_{11}+C_{22}-2C_{12}+4C_{66})$
L	$\frac{1}{2}(C_{44}+C_{55})$
F	$\frac{1}{2}(C_{11}+C_{23})$
(Degree 1)	
J_c	$\frac{1}{8}(3C_{15}+C_{25}+C_{46})$
J_s	$\frac{1}{8}(C_{14}+3C_{24}+2C_{56})$
K_c	$\frac{1}{8}(3C_{15}+C_{25}+2C_{46}-4C_{35})$
K_s	$\frac{1}{8}(3C_{14}+3C_{24}+2C_{56}-4C_{34})$
M_c	$\frac{1}{4}(C_{15}-C_{25}+2C_{46})$
M_s	$\frac{1}{4}(C_{14}-C_{24}-2C_{56})$
(Degree 2)	
B_c	$\frac{1}{2}(C_{11}-C_{22})$
B_s	$-(C_{16}+C_{26})$
H_c	$\frac{1}{2}(C_{13}-C_{23})$
H_s	$-C_{36}$
G_c	$\frac{1}{2}(C_{55}-C_{44})$
G_s	$-C_{45}$
(Degree 3)	
D_c	$\frac{1}{4}(C_{15}-C_{25}-2C_{46})$
D_s	$\frac{1}{4}(C_{14}-C_{24}+2C_{56})$
(Degree 4)	
E_c	$\frac{1}{8}(C_{11}+C_{22}-2C_{12}-4C_{66})$
E_s	$\frac{1}{2}(C_{16}-C_{26})$

Table A1. Asymptotic parameters expressed as independent linear combinations of the 21 elastic constants. Note that several asymptotic parameters may depend on one or more of the same elastic coefficients. Hence, for instance, the A kernel is $K_A = K_{C_{11}} + K_{C_{12}} + K_{C_{22}} \neq \frac{1}{8}(3K_{C_{11}} + 3K_{C_{22}} + 2K_{C_{12}} + 4K_{C_{66}})$.

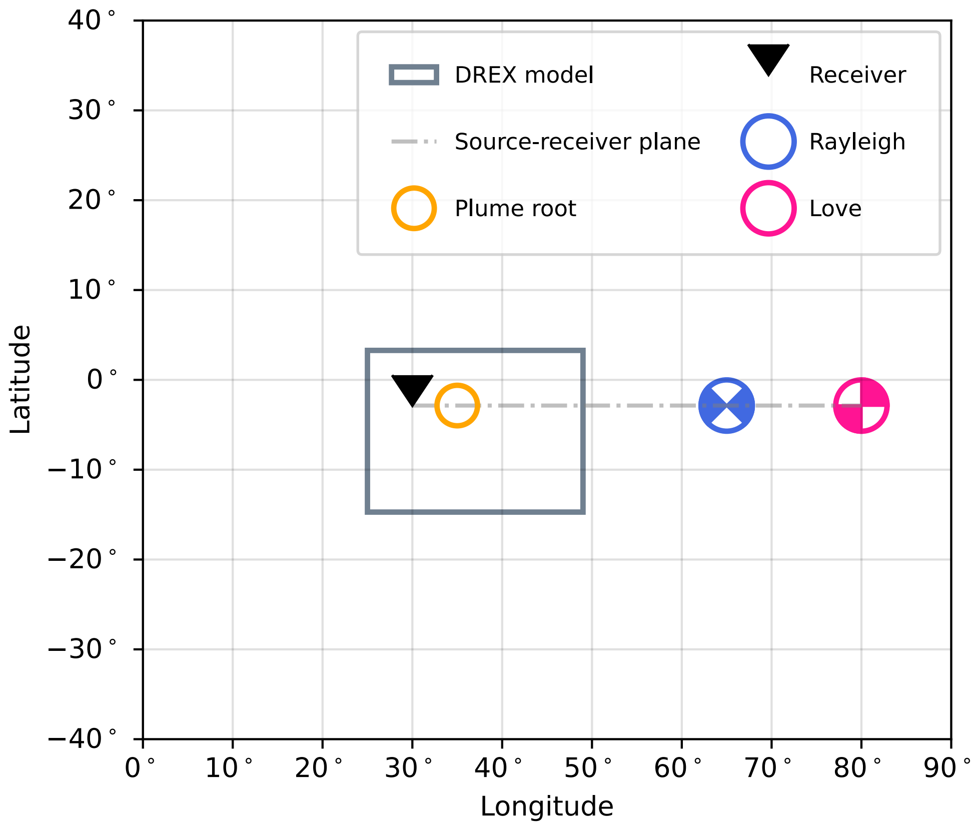

Figure A2. Schematic map view of the computational setup. Plot boundaries correspond to the size of the mesh. The smaller box outlines the original DREX model boundaries. Beachballs indicate the different source mechanisms used for Love and Rayleigh runs.

Surface-wave sensitivity to anisotropy in a 3D seismo-geodynamics mantle plume model: supplementary material

M. Desiderio, A. M. G. Ferreira, S. P. Hicks,
M. Faccenda, F. Rappisi, A. Manjón-Cabeza Córdoba, M. D. Ballmer

[1] Department of Earth Sciences, University College London, London, United Kingdom

E-mail: matteo.desiderio.20@ucl.ac.uk

[2] Dipartimento di Geoscienze, Università di Padova, Italy

[3] Istituto Nazionale di Geofisica e Vulcanologia, Sezione Bologna, Italy

[4] European Center for Geodynamics and Seismology, Luxembourg, Luxembourg

S1 Fundamental-mode, Rayleigh-wave amplitude kernels (radial component)

Figs. S1, S2, S3 show amplitude kernels for fundamental-mode Rayleigh waves in the east component (for Love, and even- and odd-degree azimuthal anisotropy parameters, respectively).

S2 Fundamental-mode, Love-wave amplitude kernels (full library)

Figs. S4, S5, S6 show amplitude kernels for fundamental-mode Love waves in the north component (for Love, and even- and odd-degree azimuthal anisotropy parameters, respectively).

S3 Phase kernels

Here, phase kernels for fundamental-mode Rayleigh and Love waves are collected (Subsections S3.1 and S3.2, respectively).

S3.1 Phase: fundamental-mode Rayleigh waves

Figs. S7, S9, S11 show kernels for Rayleigh-wave phase measurements on the vertical component. Figs. S8, S10, S12 show kernels for measurements on the east component.

S3.2 Phase: fundamental-mode Love waves

Figs. S13, S14, S15 show kernels for Love wave phase measurements on the north component.

S4 Kernels of combined measurements (full library)

In this section, the full-library of kernels for combined measurements is reported.

S4.1 Cross-component phase delay differences

Figs. S16, S17, S18 show kernels for the difference between fundamental-mode, Rayleigh-wave phase measurements made on the east and vertical component.

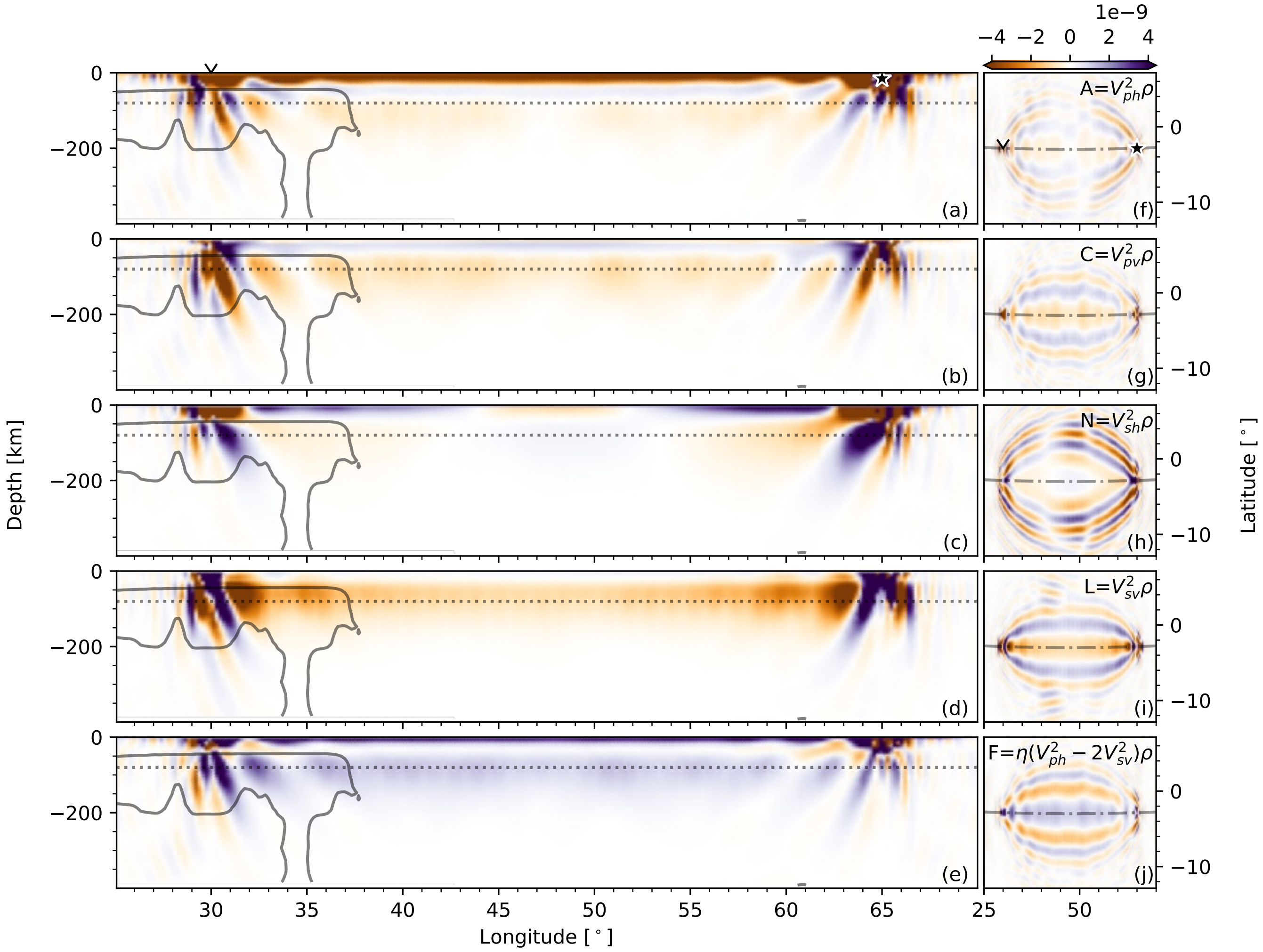

Figure S1: Amplitude kernels of radial anisotropy parameters for fundamental-mode Rayleigh-wave measurements made on the east component E, in units $\mathrm{GPa}^{-1}\mathrm{m}^{-3}$. The dotted lines in panels a-e indicate the depth ($\sim$ 80 km) at which the slices in panels f-j are taken. The dot-dashed lines in the f-j panels indicate the latitude at which the sections in panels a-e are shown, corresponding to the source-receiver plane. The maximum depth shown in the sections is 400 km, and the plume is outlined using the -0.1 % density anomaly isoline.

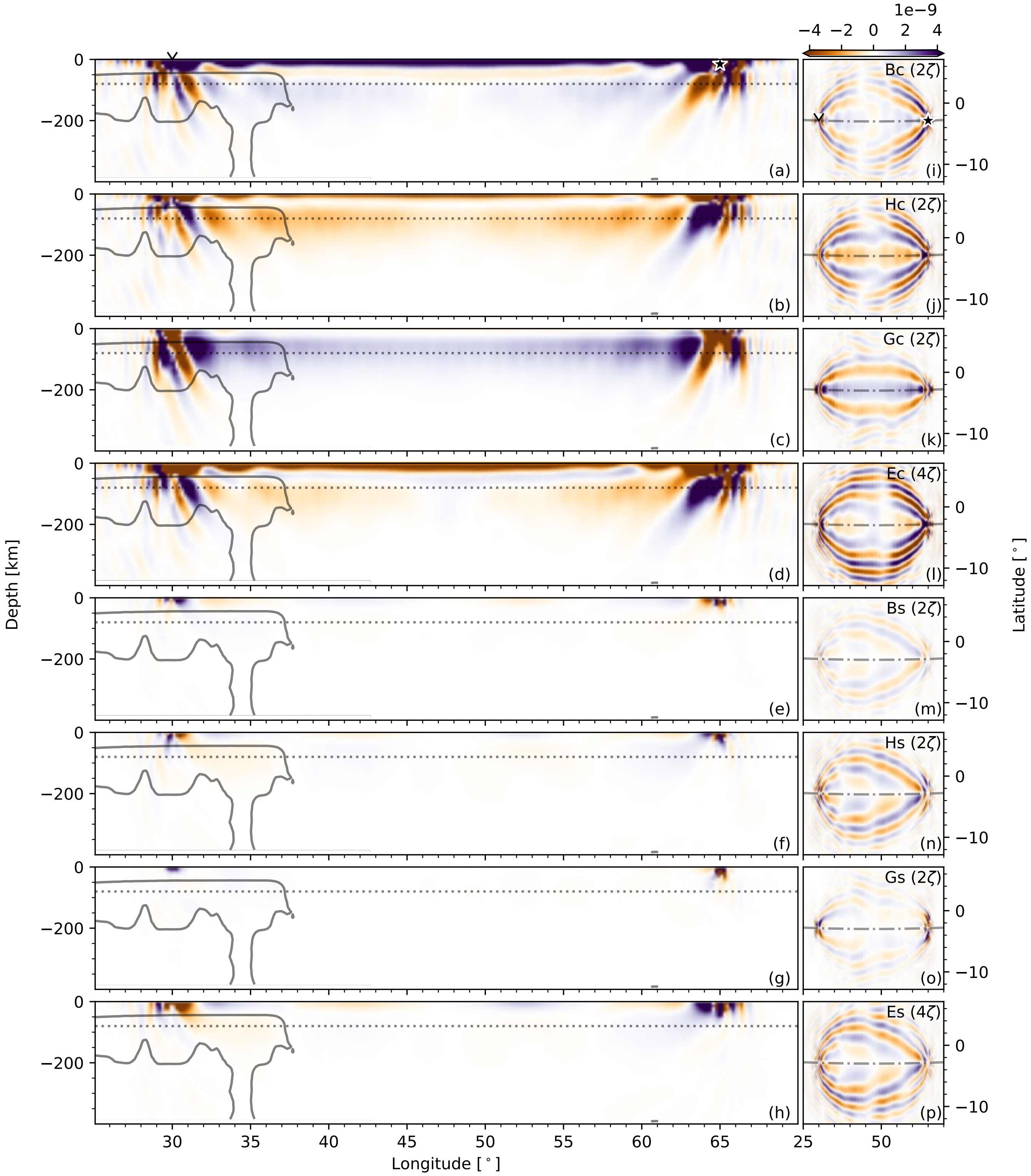

Figure S2: Amplitude kernels of even-degree azimuthal anisotropy parameters for fundamental-mode Rayleigh-wave measurements made on the east component E, in units $\mathrm{GPa}^{-1}\mathrm{m}^{-3}$. All other details as in Fig. S1.

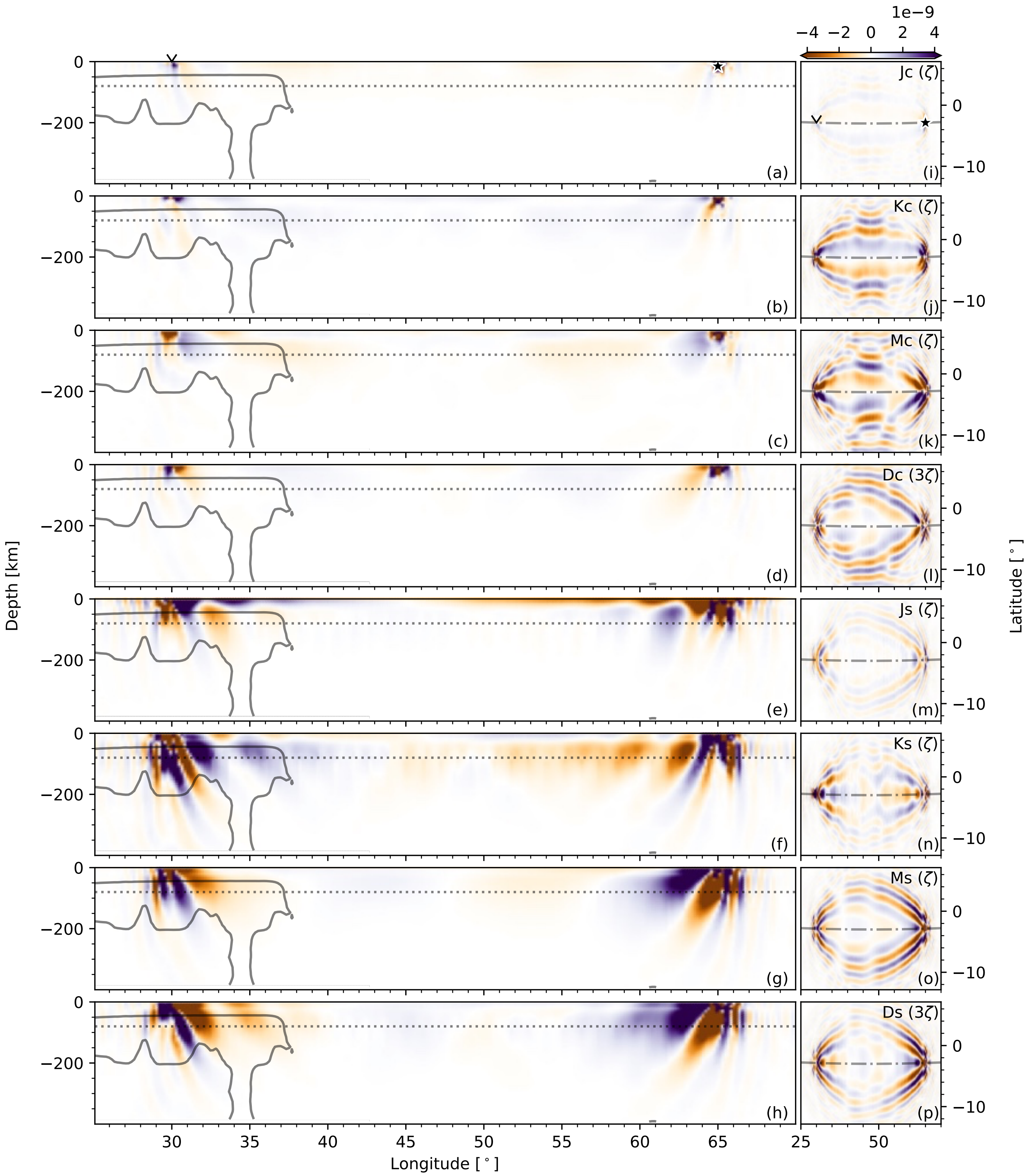

Figure S3: Amplitude kernels of odd-degree azimuthal anisotropy parameters for fundamental-mode Rayleigh-wave measurements made on the east component E, in units $\mathrm{GPa}^{-1}\mathrm{m}^{-3}$. All other details as in Fig. S1.

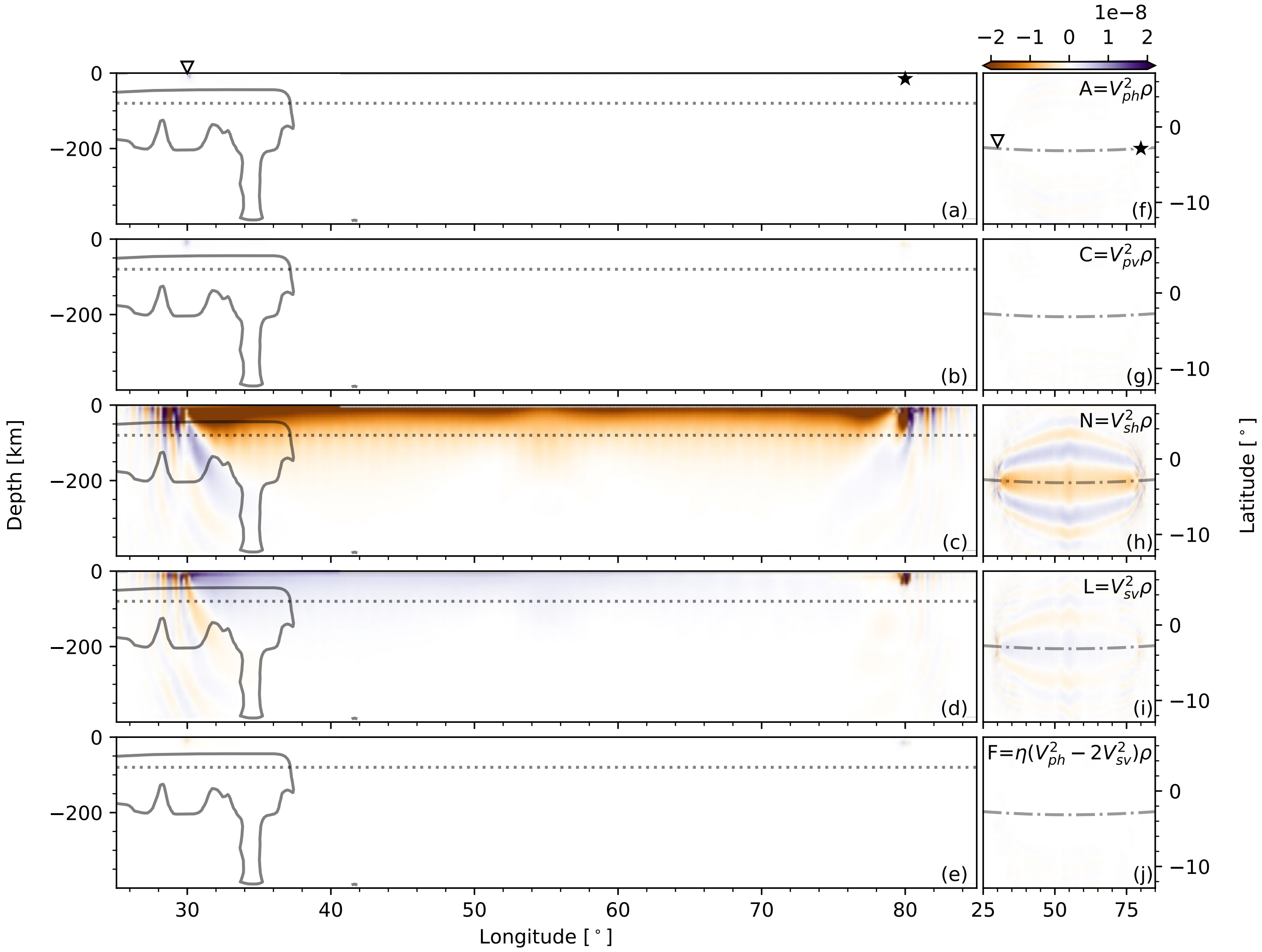

Figure S4: Amplitude kernels of radial anisotropy parameters for fundamental-mode Love-wave measurements made on the north component N, in units $\mathrm{GPa}^{-1}\mathrm{m}^{-3}$. All other details as in Fig. S1.

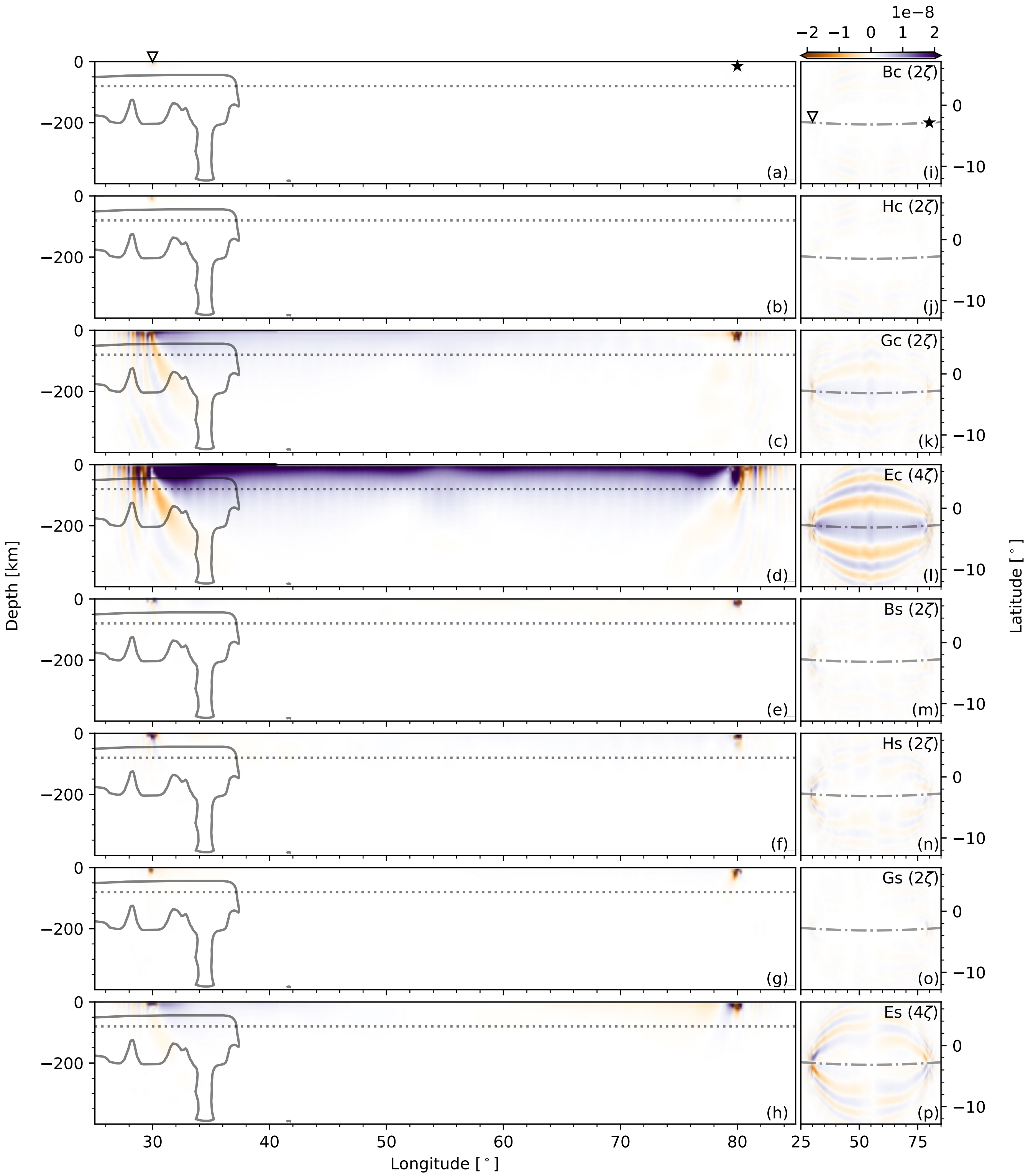

Figure S5: Amplitude kernels of even-degree azimuthal anisotropy parameters for fundamental-mode Love-wave measurements, in units $\mathrm{GPa}^{-1}\mathrm{m}^{-3}$. All other details as in Fig. S1.

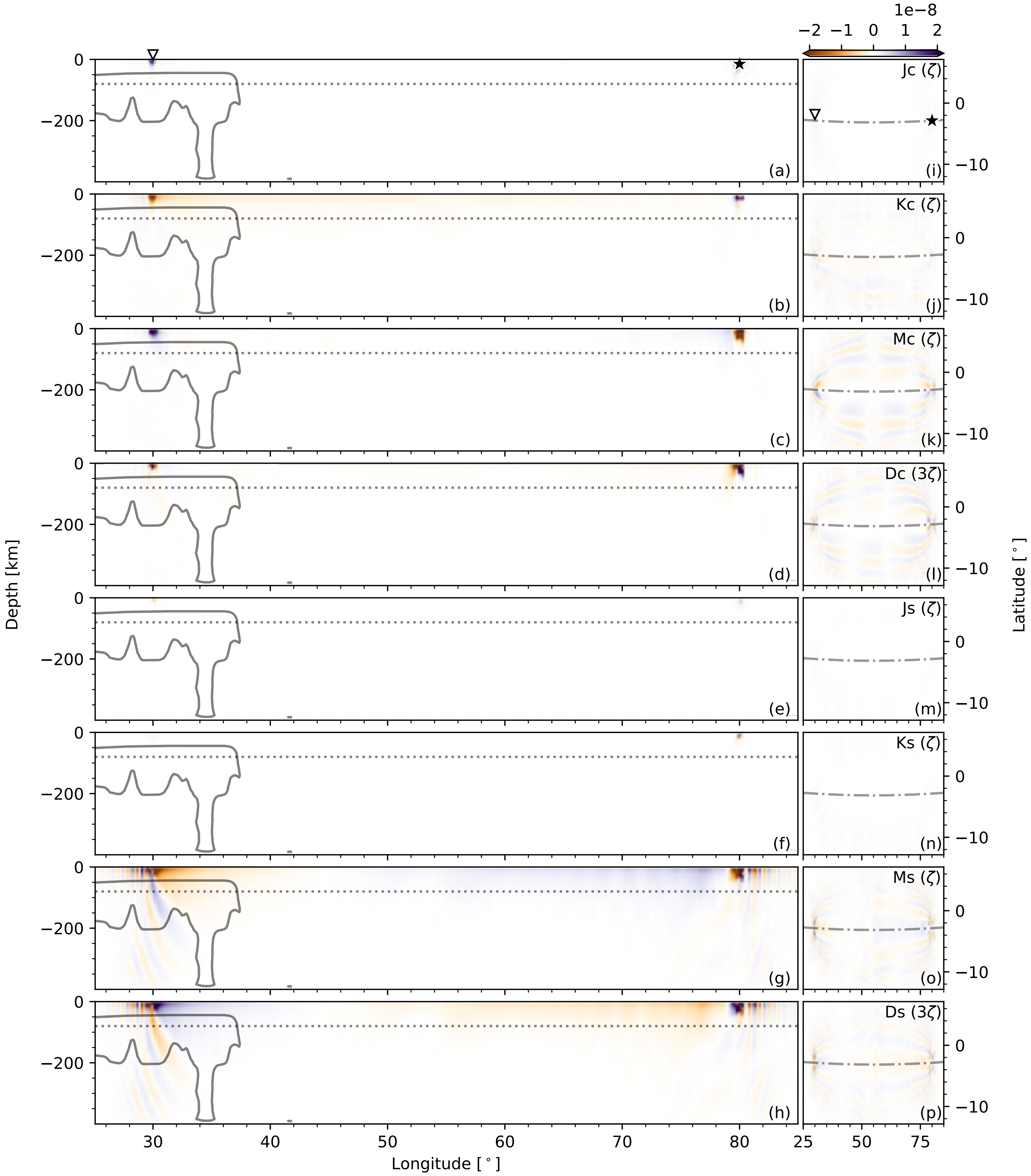

Figure S6: Amplitude kernels of odd-degree azimuthal anisotropy parameters for fundamental-mode Love-wave measurements, in units $\mathrm{GPa}^{-1}\mathrm{m}^{-3}$. All other details as in Fig. S1.

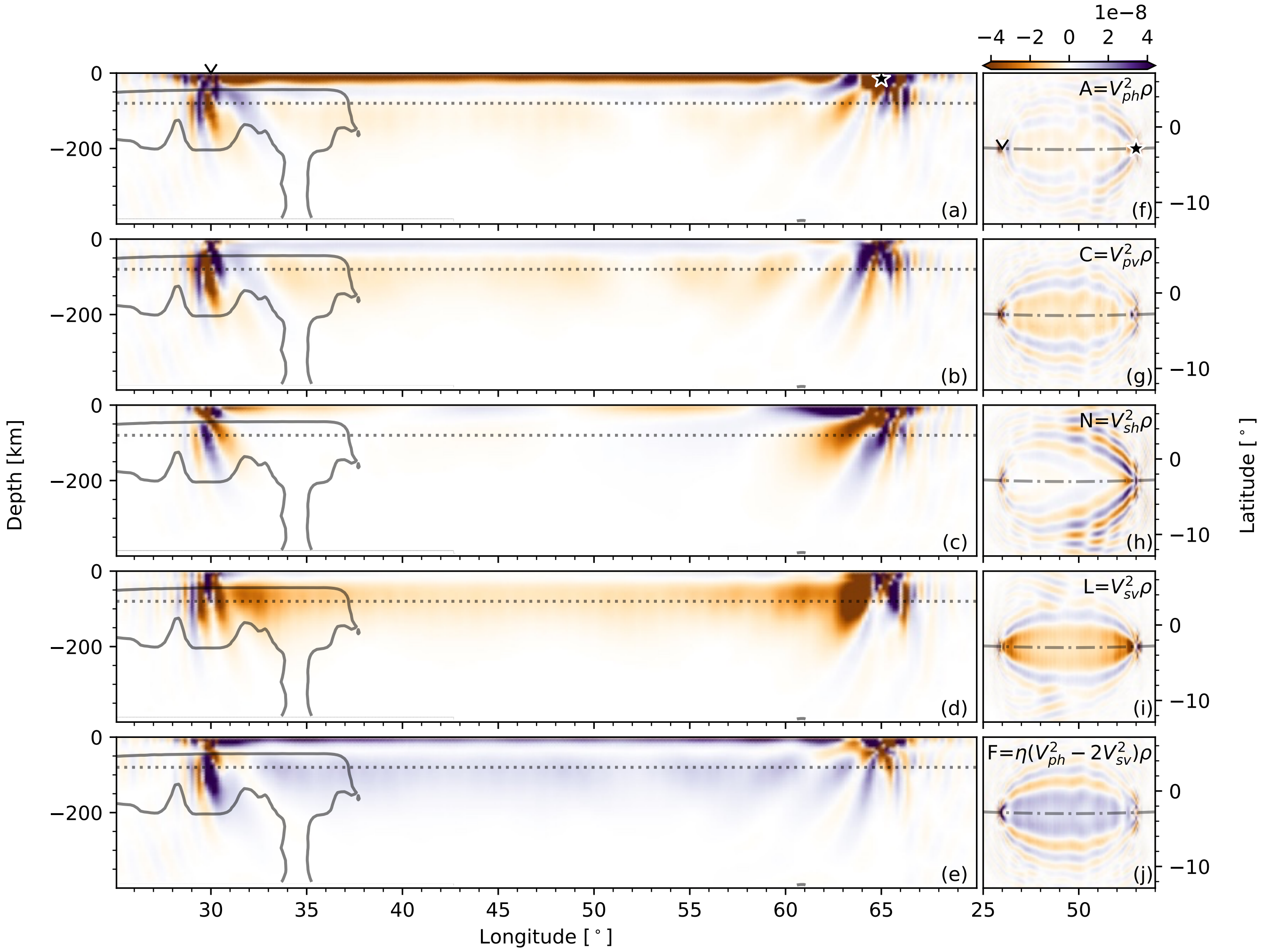

Figure S7: Phase kernels of radial anisotropy parameters for fundamental-mode Rayleigh-wave measurements made on the vertical component Z, in units s $\mathrm{GPa}^{-1}\mathrm{m}^{-3}$. All other details as in Fig. S1.

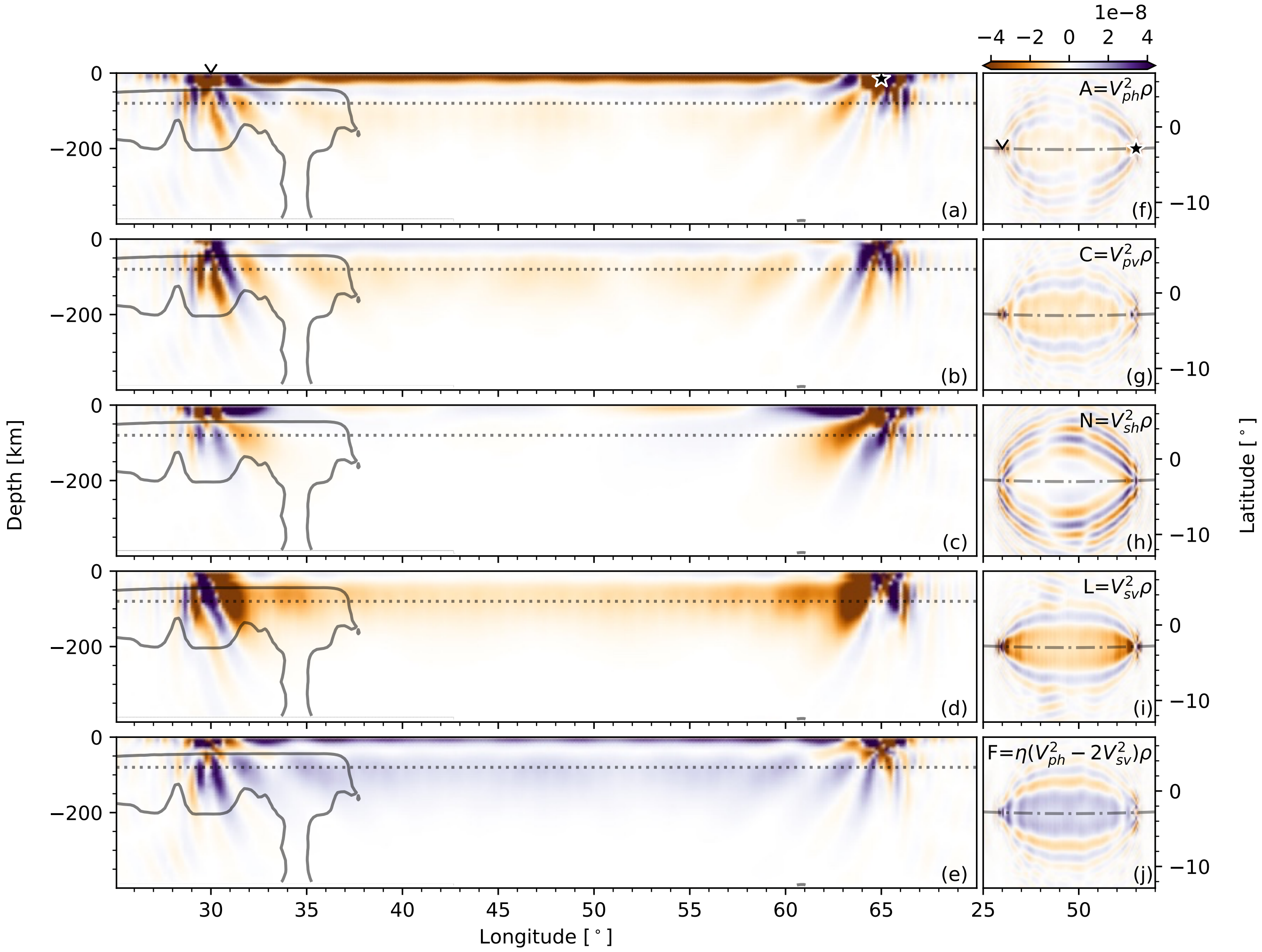

Figure S8: Phase kernels of radial anisotropy parameters for fundamental-mode Rayleigh-wave measurements made on the east component E, in units s $\mathrm{GPa}^{-1}\mathrm{m}^{-3}$. All other details as in Fig. S1.

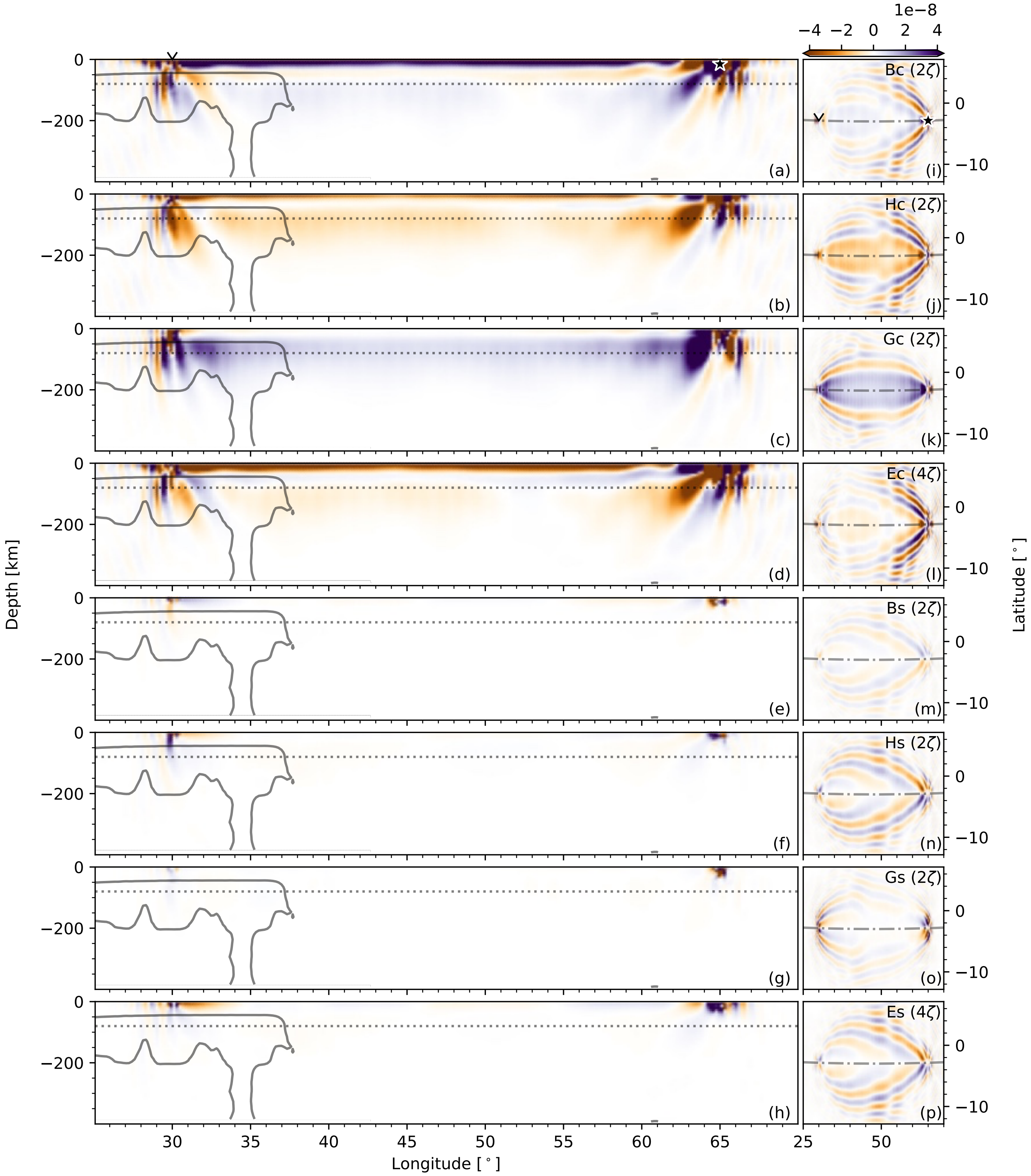

Figure S9: Phase kernels of even-degree azimuthal anisotropy parameters for fundamental-mode Rayleigh-wave measurements made on the vertical component Z, in units s $\mathrm{GPa}^{-1}\mathrm{m}^{-3}$. All other details as in Fig. S1.

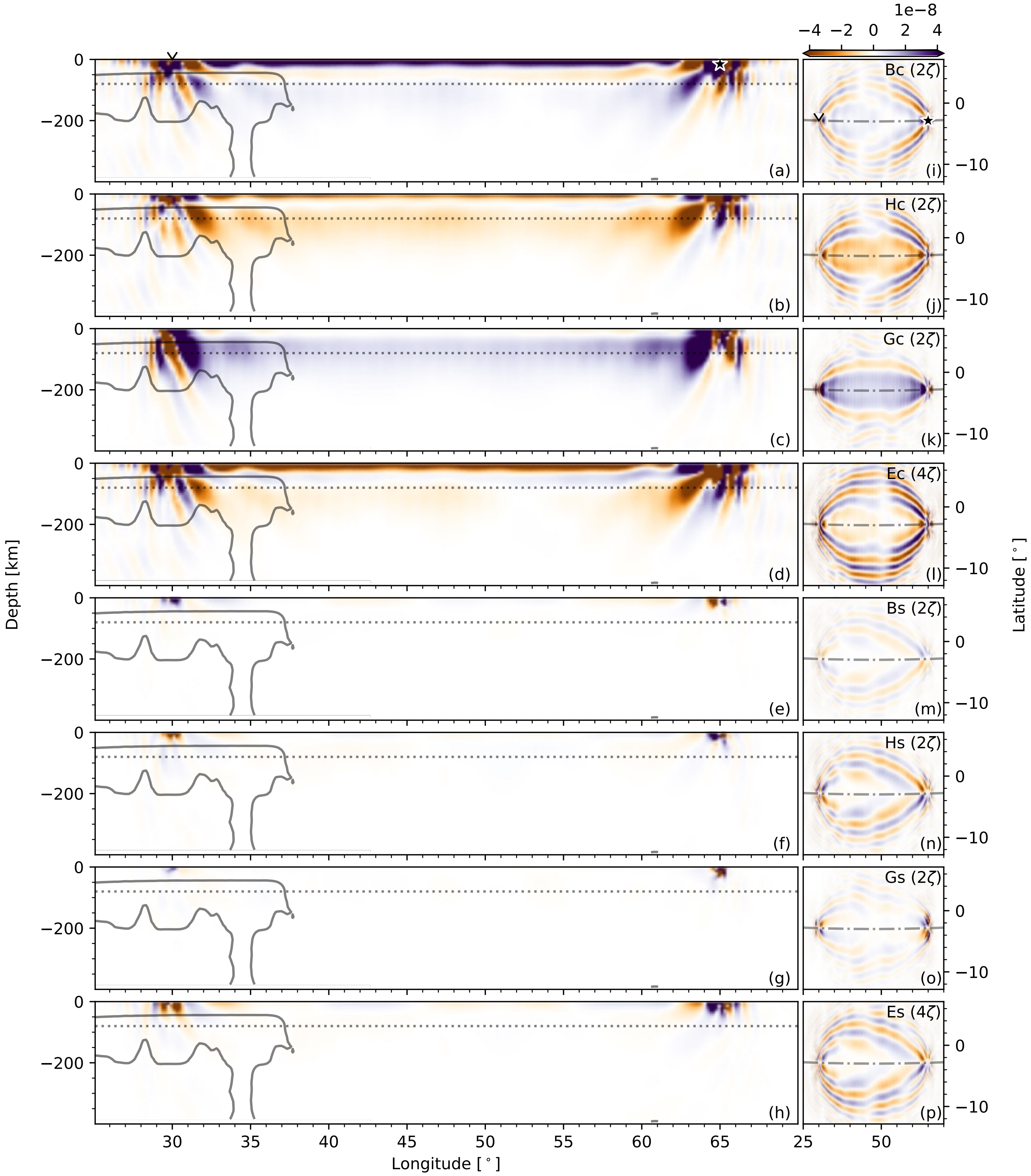

Figure S10: Phase kernels of even-degree azimuthal anisotropy parameters for fundamental-mode Rayleigh-wave measurements made on the east component E, in units s $\mathrm{GPa}^{-1}\mathrm{m}^{-3}$. All other details as in Fig. S1.

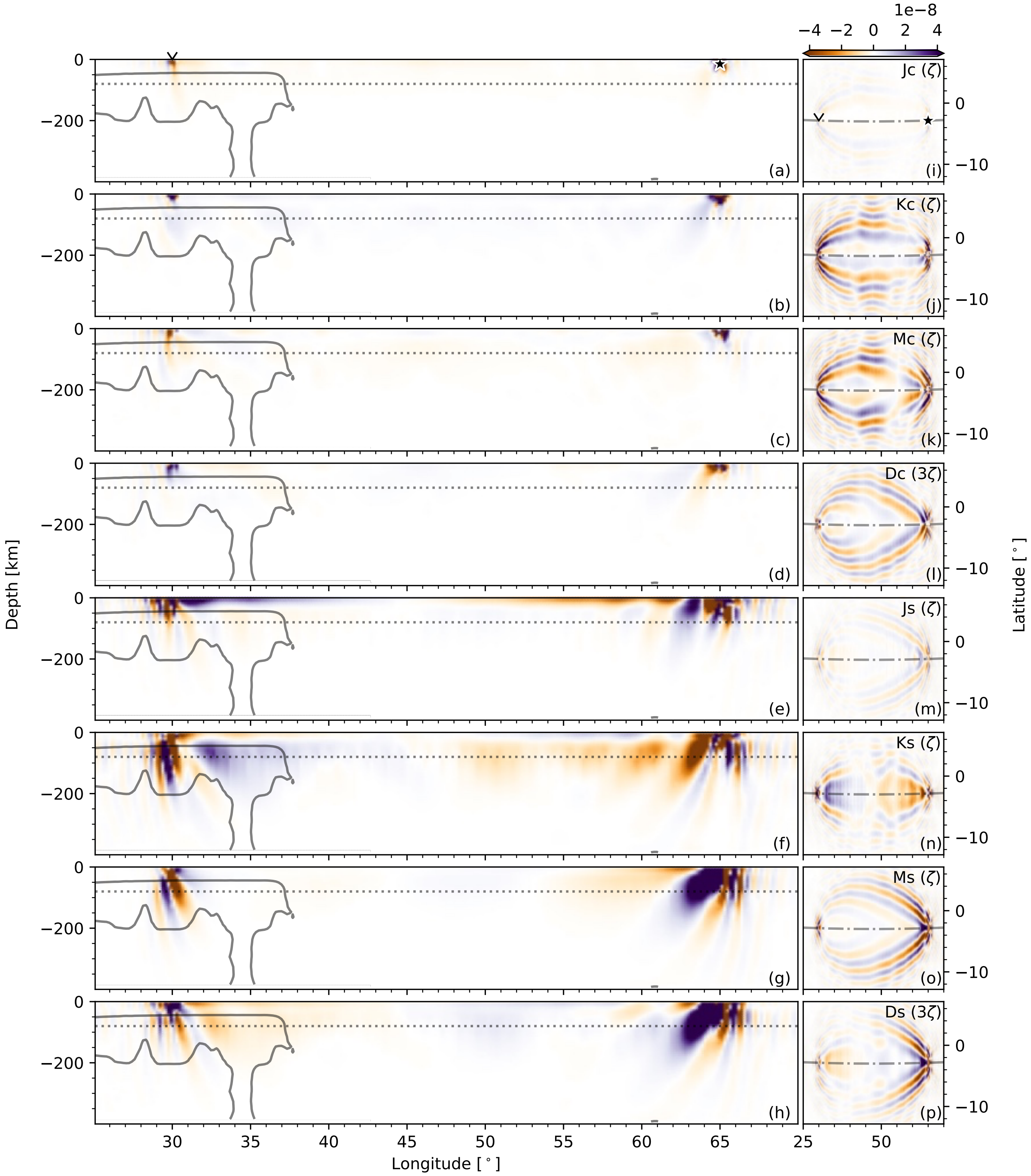

Figure S11: Phase kernels of odd-degree azimuthal anisotropy parameters for fundamental-mode Rayleigh-wave measurements made on the vertical component Z, in units s $GPa^{-1}m^{-3}$. All other details as in Fig. S1.

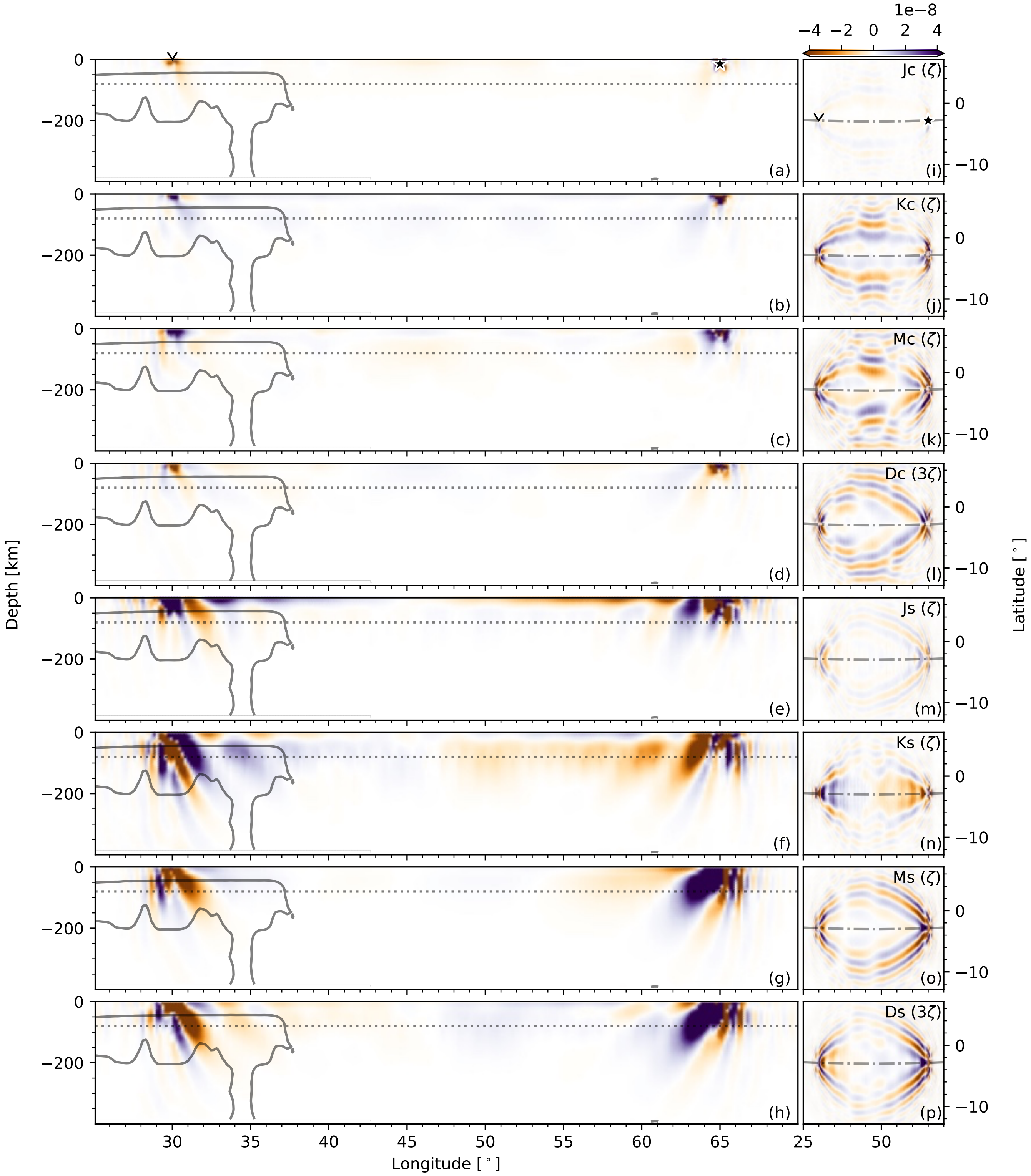

Figure S12: Phase kernels of odd-degree azimuthal anisotropy parameters for fundamental-mode Rayleigh-wave measurements made on the east component E, in units s GPa^{-1}m^{-3}. All other details as in Fig. S1.

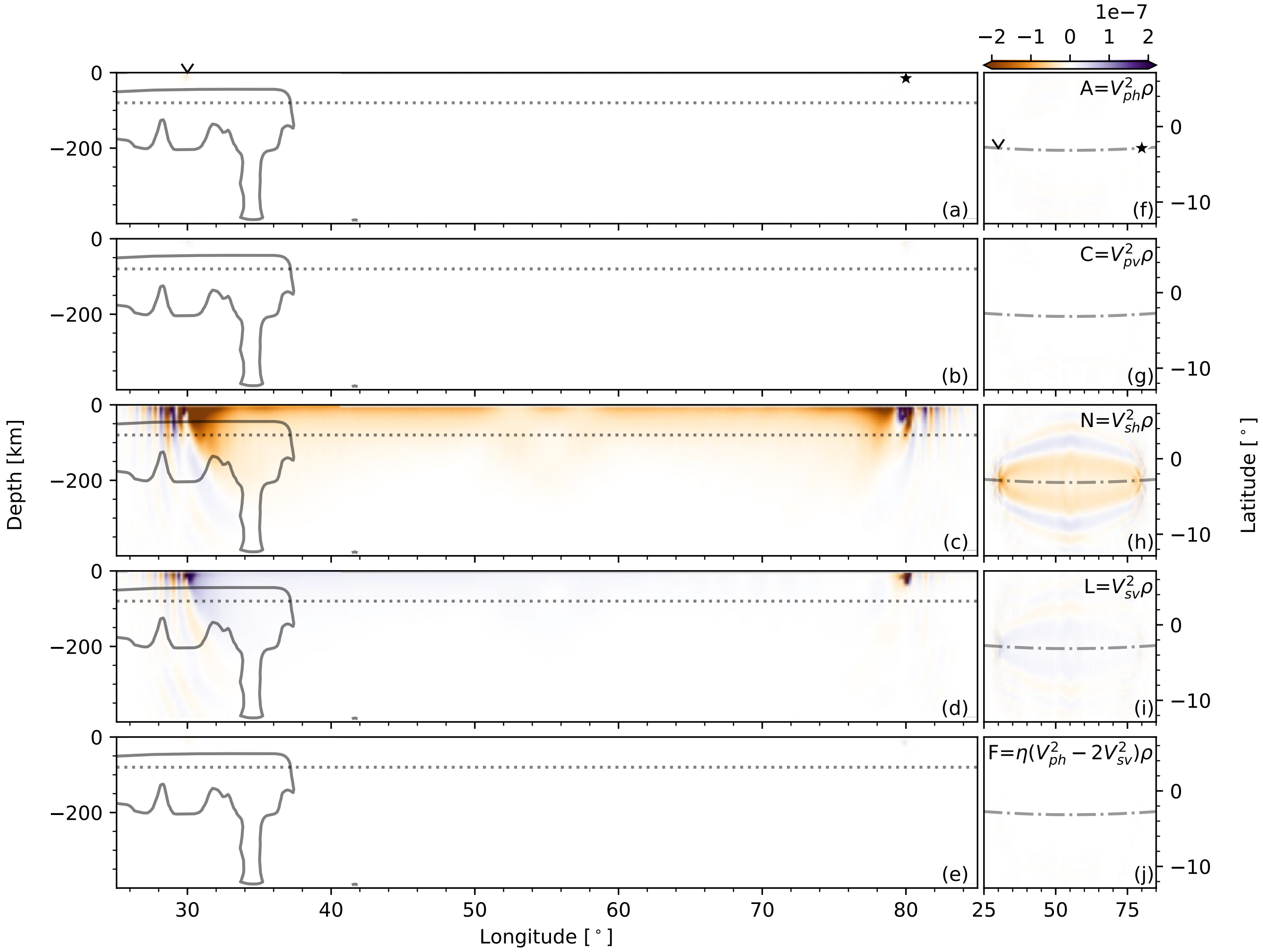

Figure S13: Phase kernels of radial anisotropy parameters for fundamental-mode Love-wave measurements, in units s $GPa^{-1}m^{-3}$. All other details as in Fig. S1.

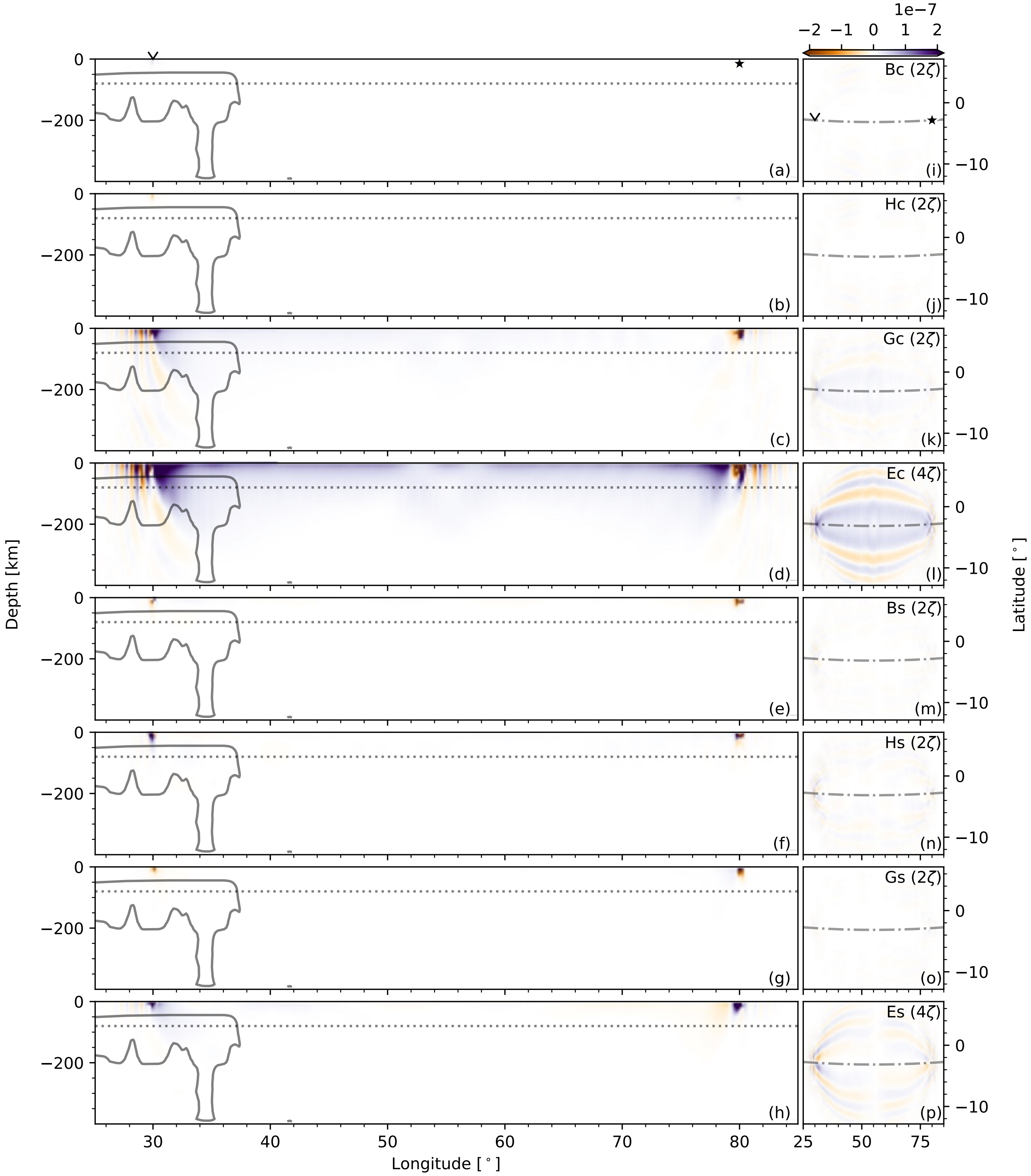

Figure S14: Phase kernels of even-degree azimuthal anisotropy parameters for fundamental-mode Love-wave measurements, in units s $\mathrm{GPa}^{-1}\mathrm{m}^{-3}$. All other details as in Fig. S1.

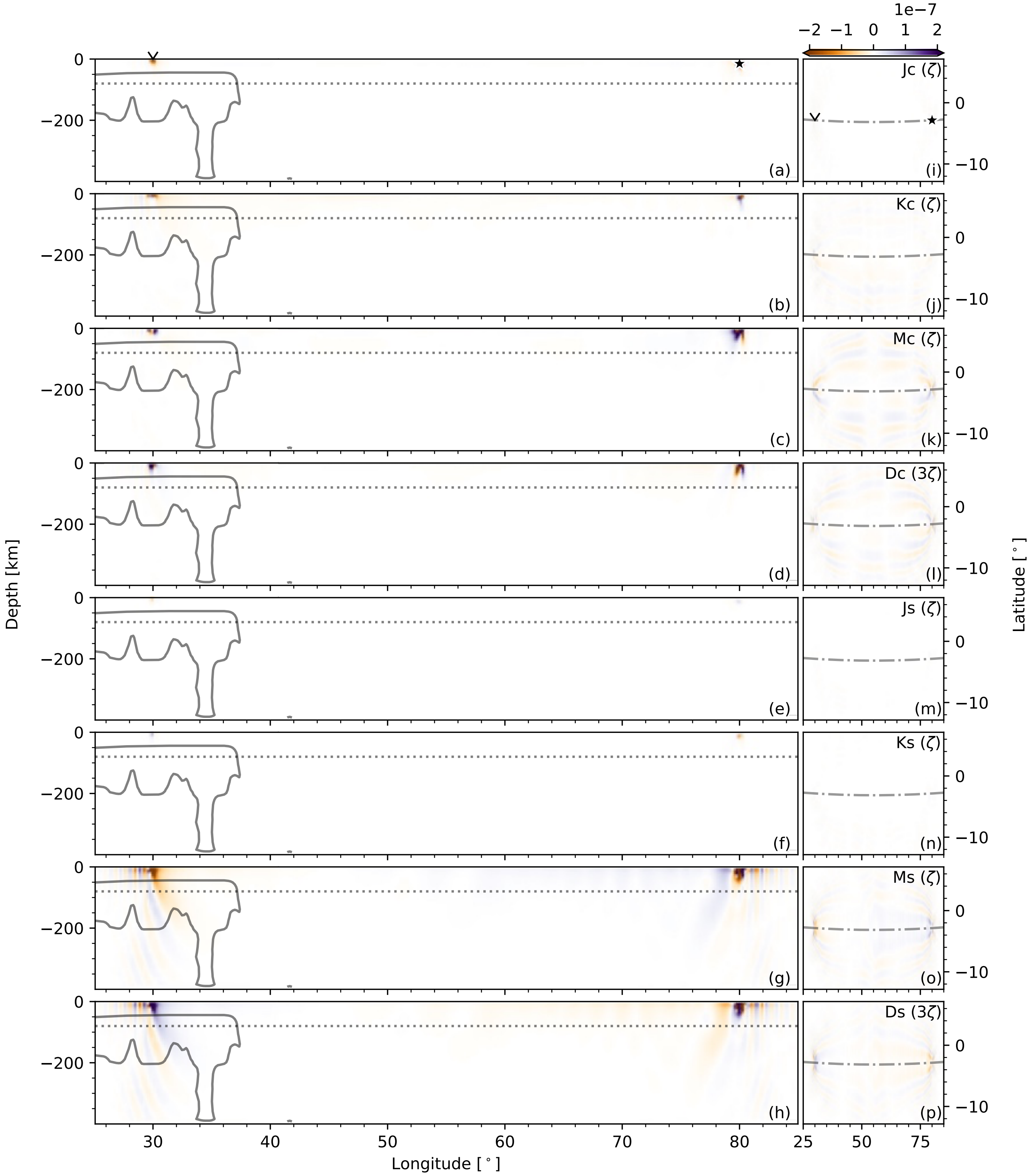

Figure S15: Phase kernels of odd-degree azimuthal anisotropy parameters for fundamental-mode Love-wave measurements, in units s $\mathrm{GPa}^{-1}\mathrm{m}^{-3}$. All other details as in Fig. S1.

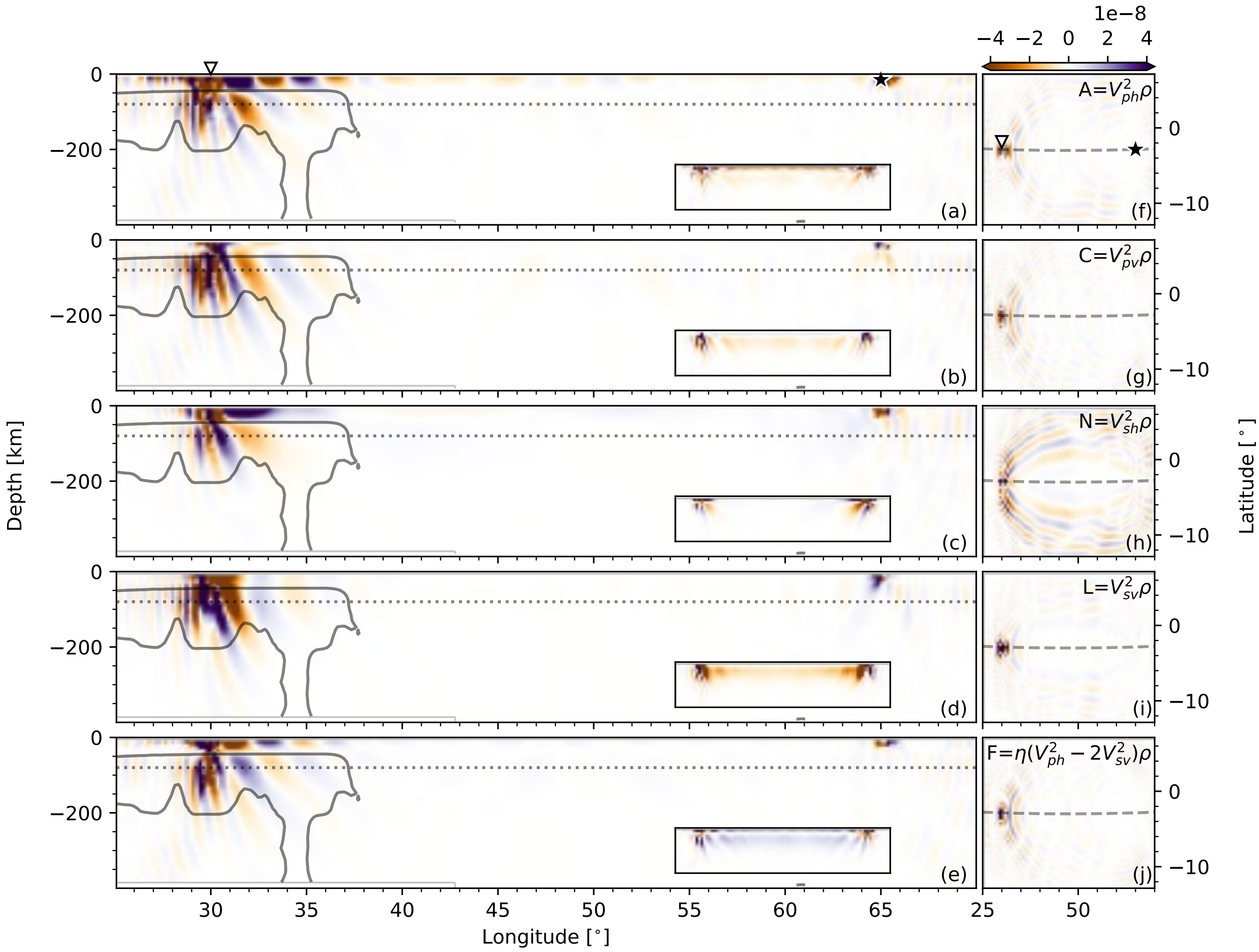

Figure S16: Kernels of differences between phase measurements made on the E and Z components, in units s $\mathrm{GPa}^{-1}\mathrm{m}^{-3}$, for radial anisotropy parameters. Kernels for E-component measurements are displayed in the insets for reference, showing that the combined measurements generally maximise the sensitivity close to the receiver. All other details are as in Fig. S1.

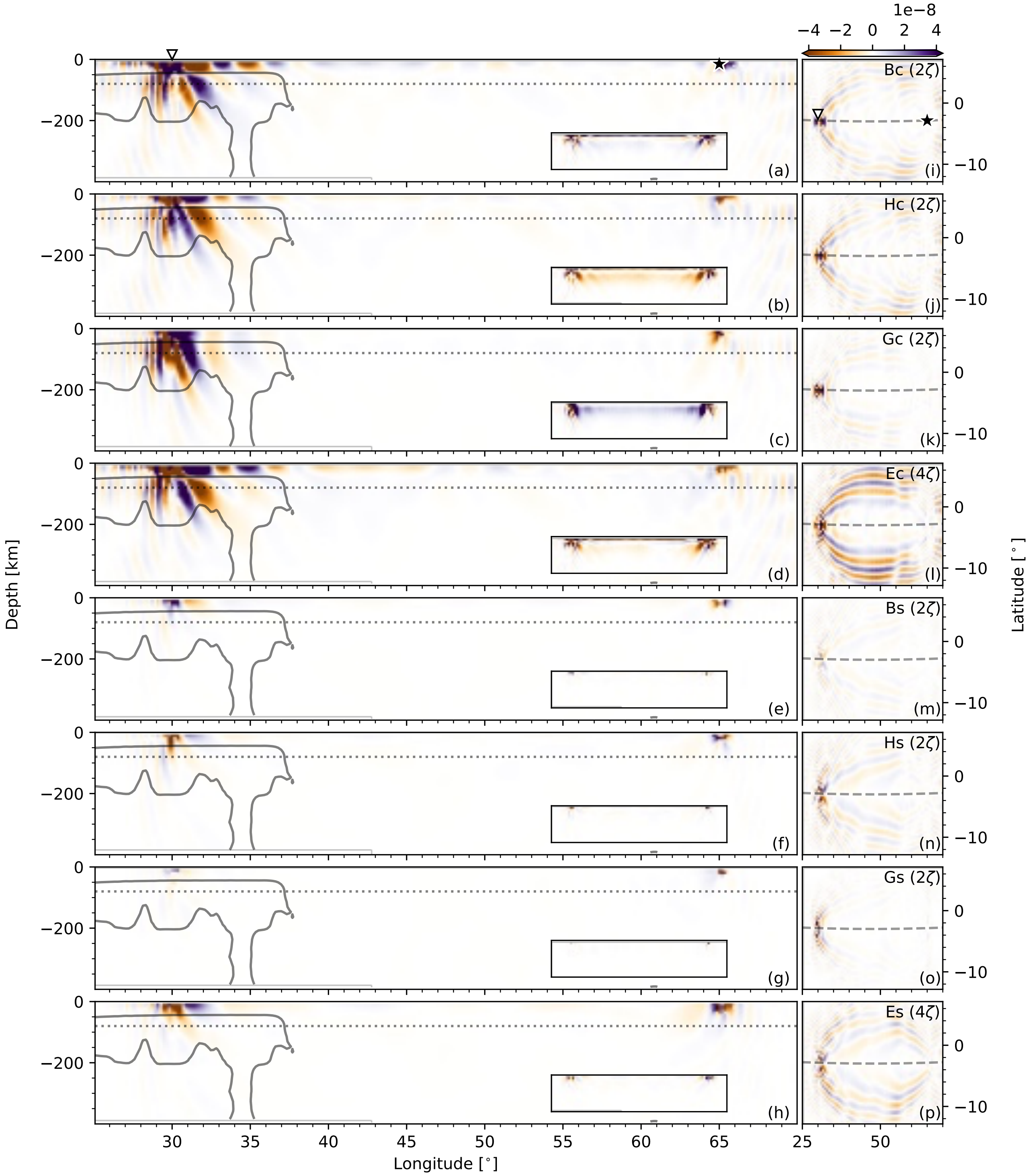

Figure S17: Same as in Fig. S16, but for even-degree azimuthal anisotropy parameters.

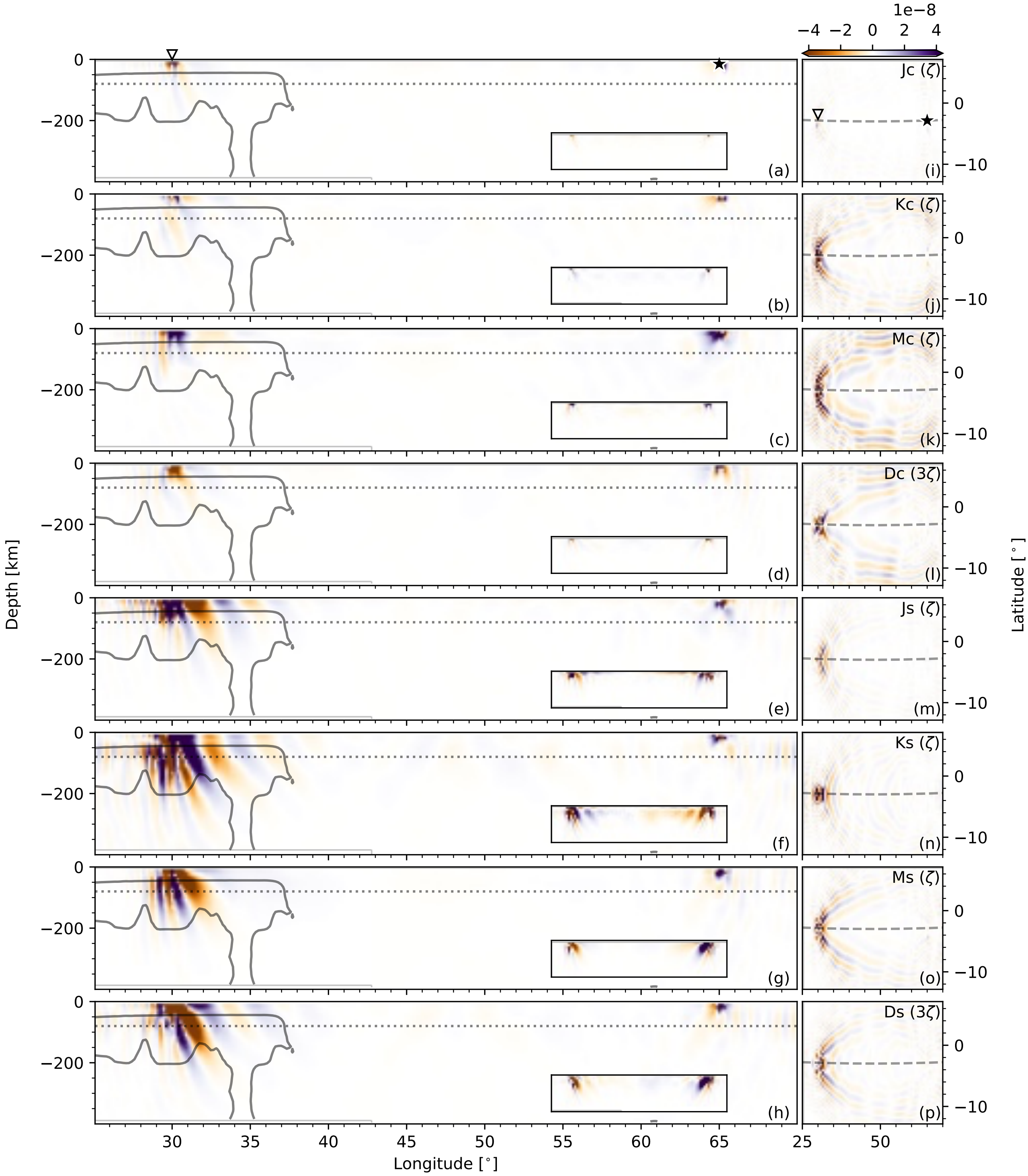

Figure S18: Same as in Fig. S16, but for odd-degree azimuthal anisotropy parameters.

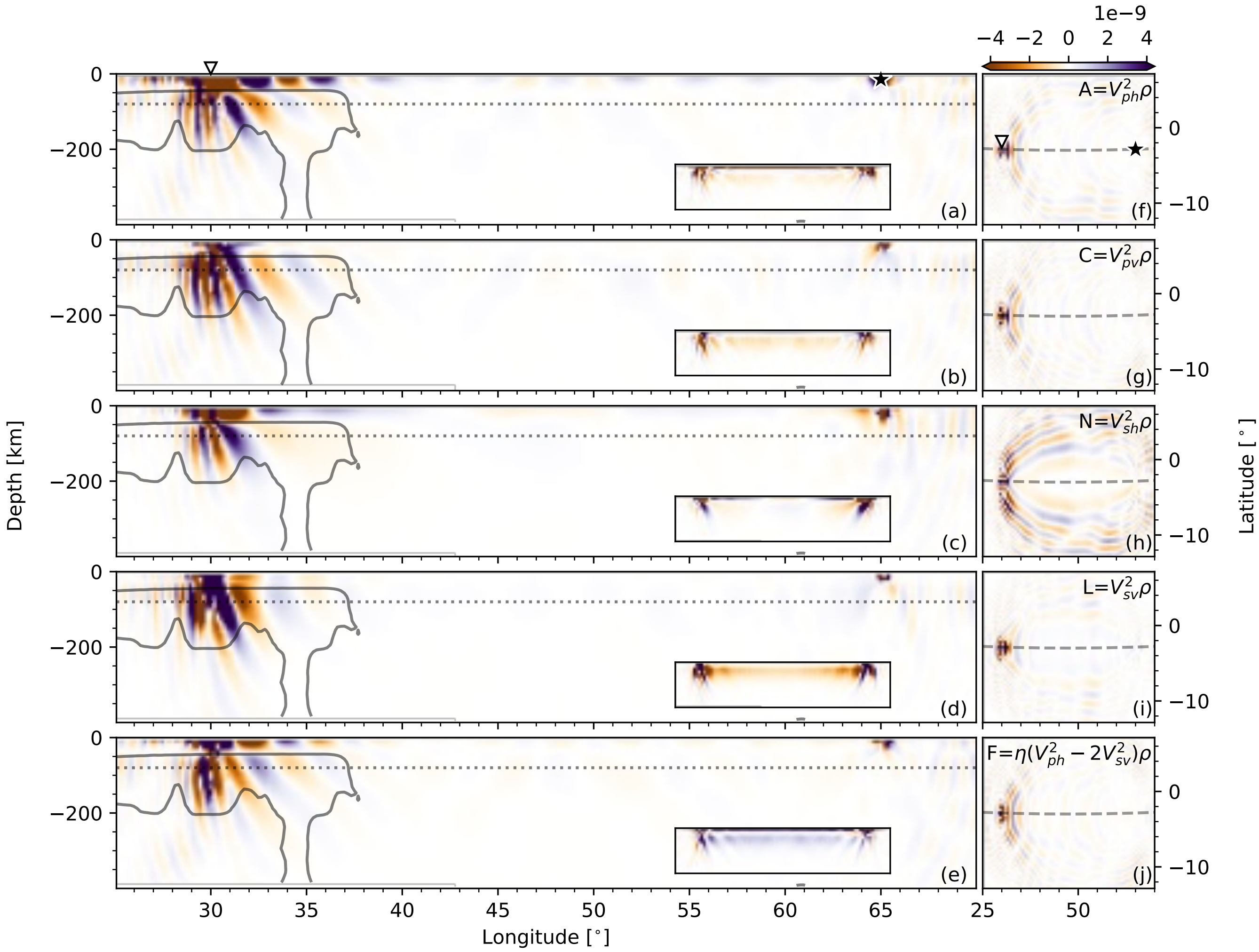

Figure S19: Kernels of differences between amplitude measurements made on the E and Z components, in units $\mathrm{GPa}^{-1}\mathrm{m}^{-3}$, for radial anisotropy parameters. Kernels for E-component measurements are displayed in the insets for reference, showing that the combined measurements generally maximise the sensitivity close to the receiver. All other details are as in Fig. S1.

S4.2 HV ratios

Figs. S19, S20, S21 show kernels for the difference between fundamental-mode, Rayleigh-wave amplitude measurements made on the east and vertical component (i.e., horizontal to vertical ratio kernels).

S5 Period band dependence

Here, the period-dependence of amplitude kernels is demonstrated by showing examples for radial-anisotropy parameters (fundamental-mode, Rayleigh-wave, vertical-component measurements only). Figs. S22, S23 show calculations using adjoint-source time-functions filtered in the 60-80 s and 80-120 s period bands, respectively. These examples demonstrate that a higher sensitivity at greater depth may be obtained by increasing the period range of the measurement. Calculations for phase kernels and for Love waves, as well as for other components and parameters are omitted for brevity, but show the same trends.

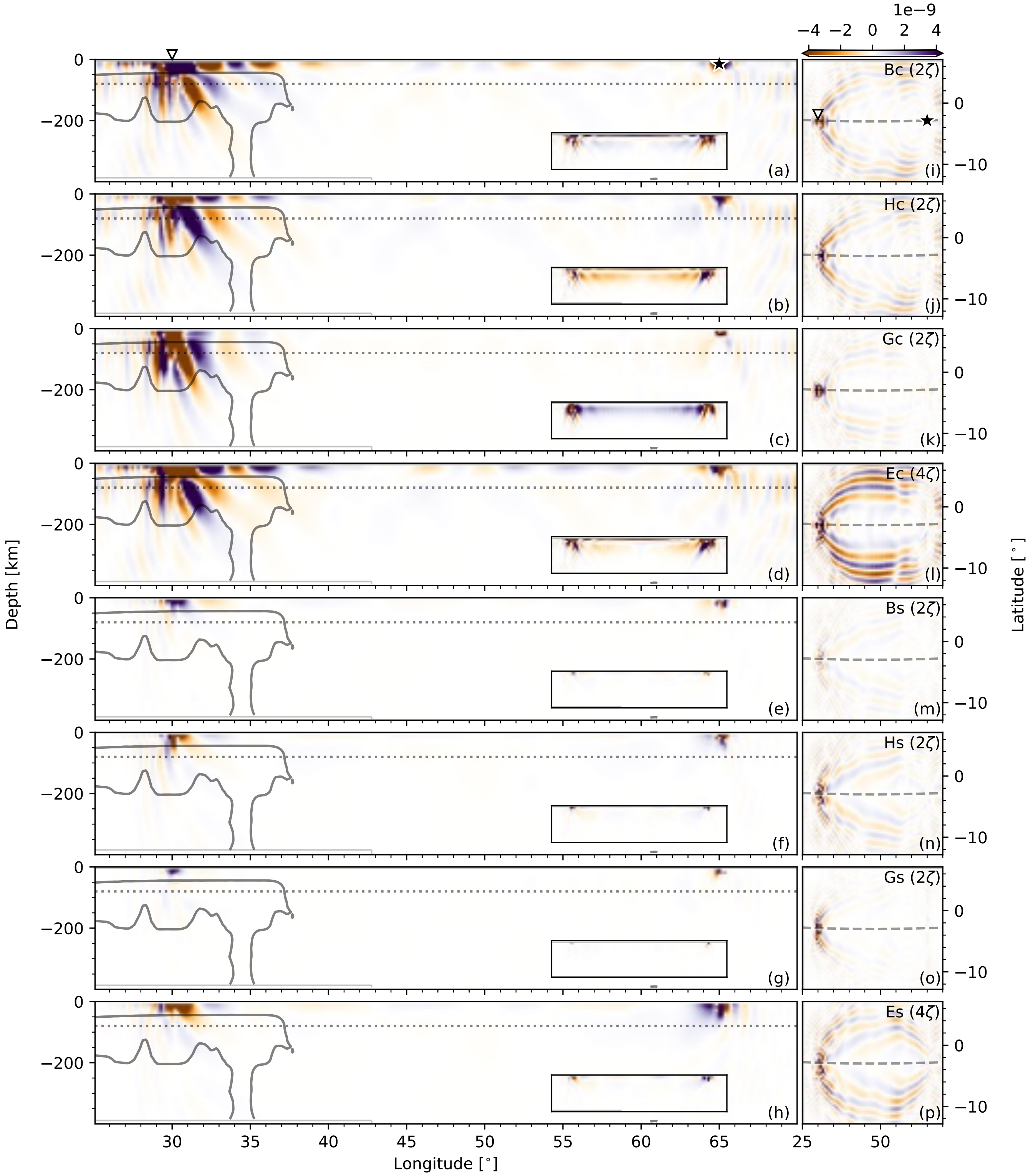

Figure S20: Same as in Fig. S19, but for even-degree azimuthal anisotropy parameters.

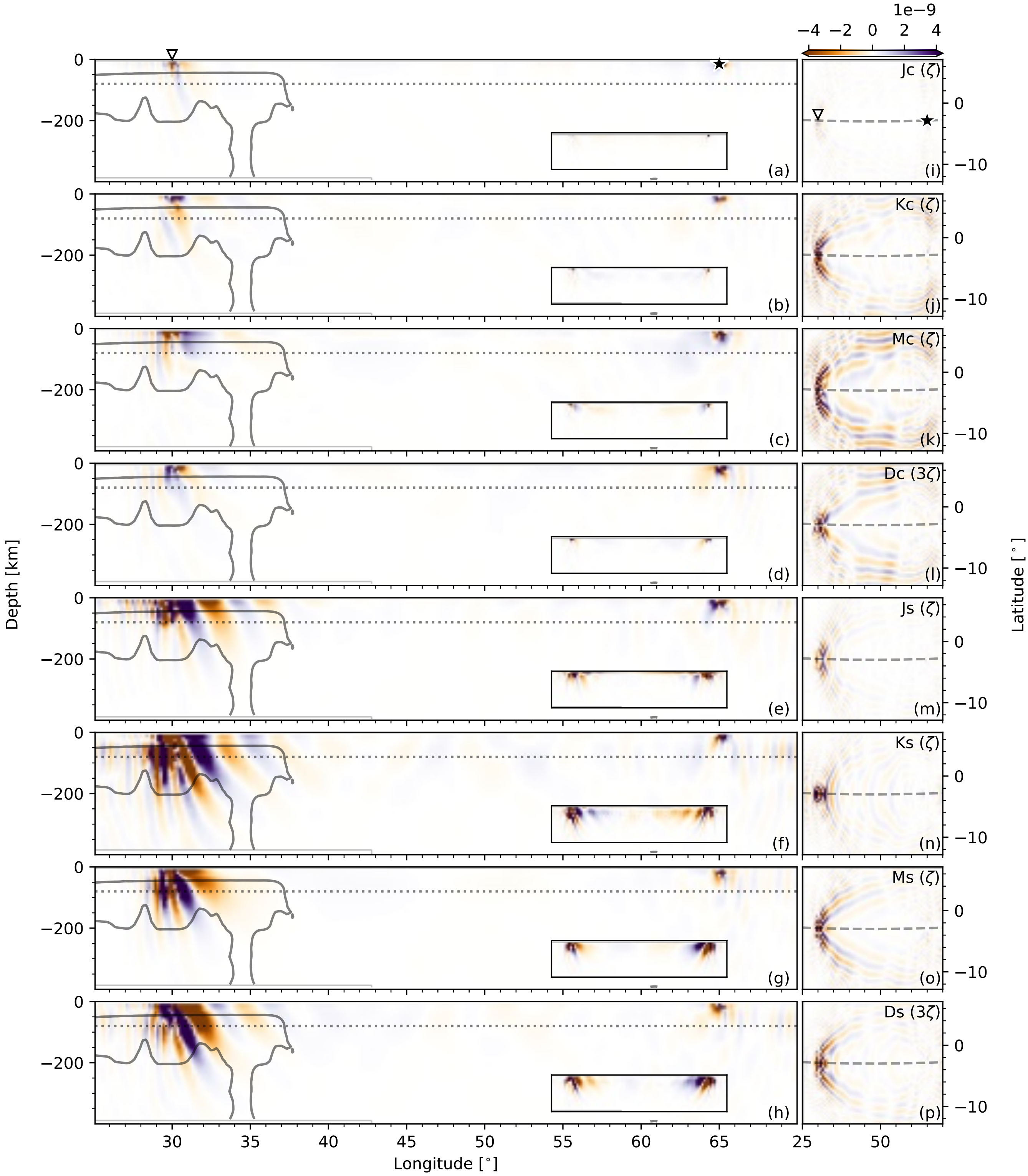

Figure S21: Same as in Fig. S19, but for odd-degree azimuthal anisotropy parameters.

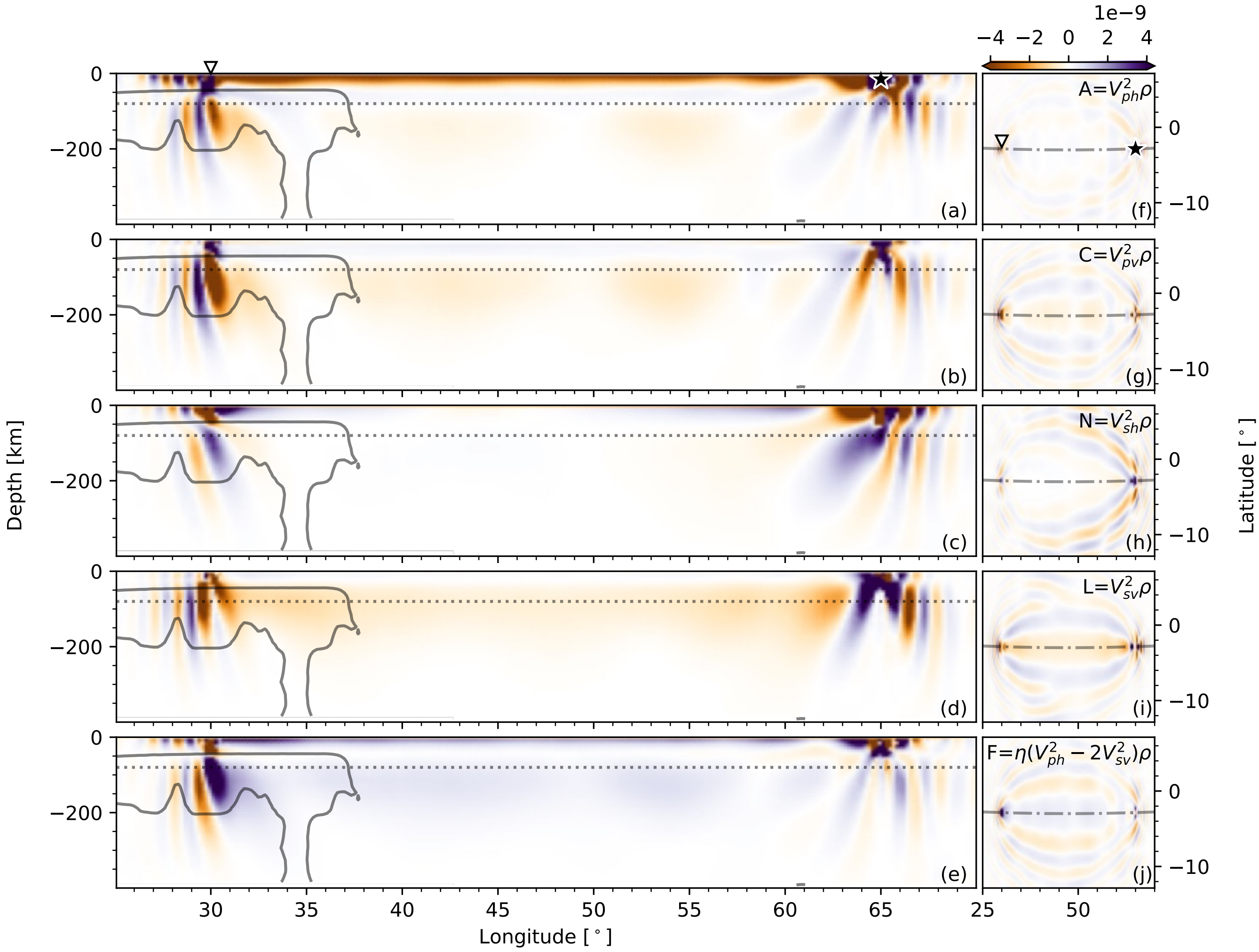

Figure S22: Same as in Fig. S1, but for measurements in the period-band 60-80 s.

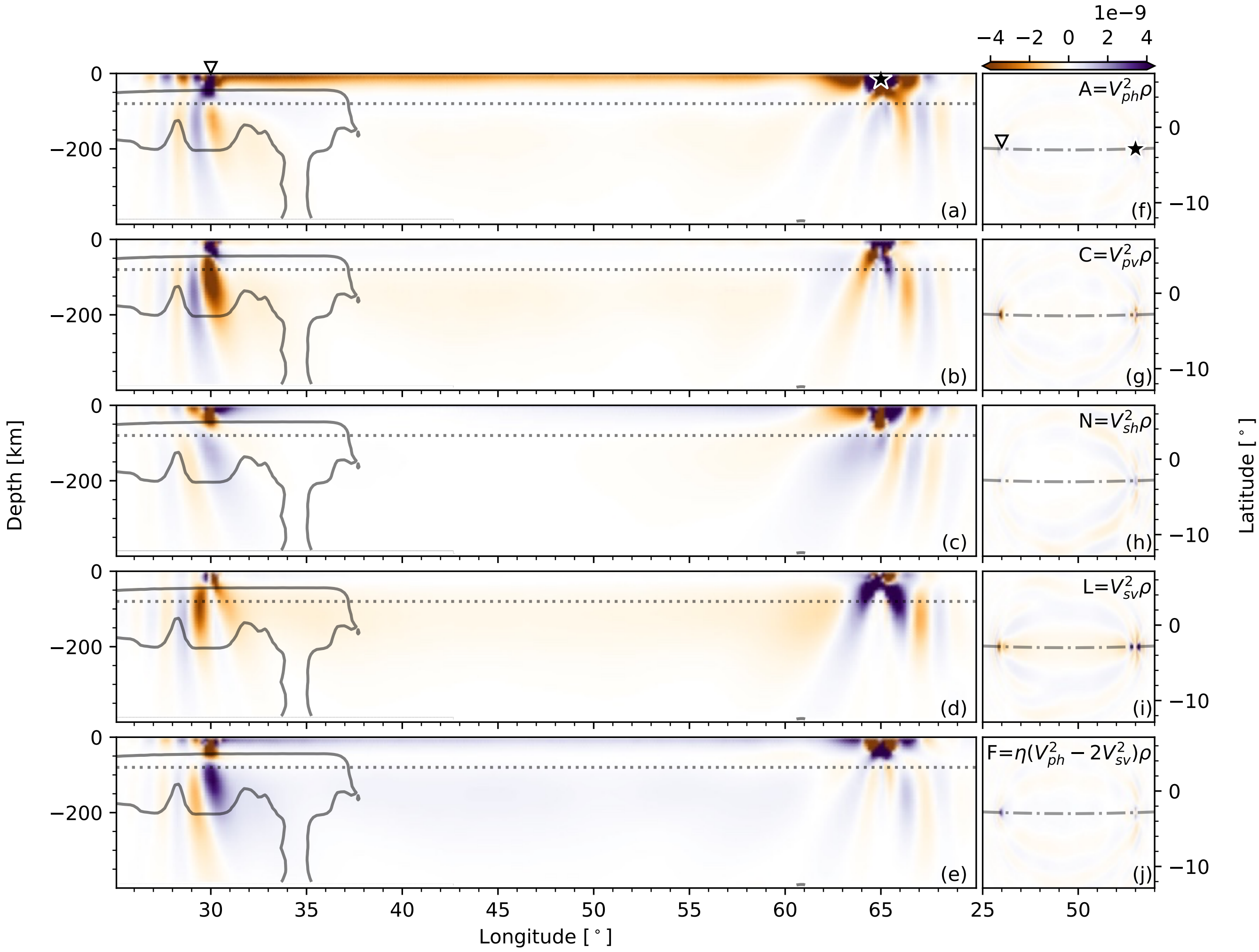

Figure S23: Same as in Fig. S1, but for measurements in the period-band 80-120 s.